Numerical Simulation Studies of Oceanic Anomalies in the North Pacific Basin. I: The Ocean Model and the Long-Term Mean State

J. C. K. HUANG[1]

Scripps Institution of Oceanography, University of California, San Diego, La Jolla, CA 92093

ABSTRACT

A three-dimensional, prognostic numerical model of the North Pacific Ocean, possessing an actual coastal configuration and ten layers (but constant depth), has been developed in order to show the physical nature of large-scale normal and abnormal characteristics of this ocean in response to various normal and anomalous seasonal meteorological conditions. Based on the simulated energetics, emphasis is given to the identification of the major physical processes and essential dynamic mechanisms responsible for the generation, evolution and dissipation of large-scale anomalies in the North Pacific Ocean. The model is based on time integrations of the finite-difference forms of the primitive equations. The oceanic circulation is driven by atmospheric forcing, namely, the surface wind stresses and the differential heating over the ocean. The flux form of numerical scheme for energy conservation and the rigid-lid approximation for filtering out the external inertia-gravity wave are used in the formulation.

The model was spun-up for more than 60 years with the annual mean atmospheric data as the forcing boundary conditions. The long-term mean state in the model reveals the large-scale features of the circulation patterns and density distributions in the North Pacific Ocean. Three gyres, one large anticyclonic in the subtropical region and two smaller ones in the subarctic and in the tropic regions, are well developed. The total transport near the western boundary reached $56 \times 10^6 \, \text{m}^3 \, \text{s}^{-1}$, which agrees reasonably well with the observed mean transport in the Kuroshio Current south of Japan. The equatorial currents, the Oyashio Current, the North Pacific Current, the Alaska Current and the California Current are simulated roughly in the model. There is upwelling along both the equator and the western boundary. Temperature and salinity distributions, except in high latitudes, compare well with observational data.

1. Introduction

In recent years, the substantial deviations of sea-surface temperatures from their long-term means (i.e., thermal anomalies in the ocean) have attracted the attention of many oceanographers and meteorologists. These anomalous phenomena, together with their temporal correlations and their spatial teleconnections with oceanic and atmospheric changes, have been extensively studied by Bjerknes (1962, 1966, 1969), by Namias (1959, 1965, 1970) and by others (e.g., Petterssen *et al.*, 1962; Rodewald, 1963). The general conclusions ascertain that the thermal anomalies in the ocean are constantly modifying the overlying atmospheric circulation, thereby altering the wind systems and the weather patterns. Observations indicate that climatic fluctuations in the ocean and atmosphere occur in all parts of the world at all times (Namias, 1965). In the Pacific Ocean, field data from the North Pacific Experiment (NORPAX) have shown that large temperature

anomalies with intensities sometimes as high as 2–5°C frequently occupy one-third to one-half or more of the North Pacific Ocean, and they usually persist for long periods of time. In addition to possible feedback to the atmosphere, the anomalies cause abnormal advection which, together with the atmospheric variations, influence the general oceanic circulation patterns (Namias, 1965; Arthur, 1966). For example, in 1957–58 an anomalous sea surface temperature in the Pacific was associated with the weakening of the California Current and a swinging of the southward flowing current offshore (Isaacs, 1968). This resulted in a strong invasion of warm, subtropical water into the west coast as far north as British Columbia.

The atmosphere and ocean are closely coupled and mutually interacting. In the large-scale air/sea interactions the ocean primarily supplies heat to the atmosphere while the atmosphere supplies momentum and heat to the ocean. The heat released from the ocean modifies the atmospheric circulation while the momentum and heat exchange from the atmosphere to the ocean determine the flow pattern and heat content in the ocean. The oceanic circulation, then, redistributes the thermal energy, thereby

---

[1] Present affiliation: Great Lakes Environmental Research Laboratory, NOAA, Ann Arbor, MI 48104, and Department of Atmospheric and Oceanic Sciences, The University of Michigan, Ann Arbor 48109.

setting up a generally closed feedback system between the ocean and the atmosphere. For the purpose of studying the mutual effects and their teleconnections in the ocean/atmosphere system, it is indispensible to employ an ocean/atmosphere coupled system. In a pioneering work, Manabe and Bryan (1969) performed the first numerical experiment of an ocean/atmosphere model that included major coupling and mutual adjusting mechanisms. Their results showed that the poleward transport of heat by oceans reduced the atmospheric meridional heat transport, which in turn decreased the baroclinic instability in the troposphere. In the tropics, the oceanic effect changed the rainfall distribution and influenced the strength of the Hadley circulation producing more realistic results. The ability of the combined ocean/atmosphere model to more accurately portray the large-scale features in the atmosphere is further demonstrated in their recent studies (Manabe et al. 1975; Bryan, et al., 1975).

Simulation studies of the ocean have been successfully carried out by Takano (1969), Il'in et al. (1969), O'Brien (1971), Bye and Sag (1972), Bryan and Cox (1972) and Holland and Hirschman (1973). These studies have taken into account realistic configurations of the ocean basins with a simplified formulation of the physics. Bryan (1963), Gormatyuk and Sarkisyan (1965), Bryan and Cox (1968), Crowley (1970) and Haney (1974) have taken more complete dynamics into account for certain idealized domains. Cox (1970) has used Bryan's model (1969), which includes the whole dynamics as well as the irregular boundaries, to investigate the monsoon effect in the circulation patterns in the Indian Ocean; and more recently Bryan et al. (1975) have coupled the ocean model with the atmospheric model to investigate world ocean circulations.

Though it is not realistic to employ a regional atmospheric model for studies of planetary responses and global teleconnections, a regional ocean model is appropriate for dynamic studies in the ocean due to its solid boundary and the semi-isolated characteristics of certain basins. If one addresses the more specific problems of physical processes, thermal structures and dynamic responses in an ocean under meteorological forcing, it is probably justifiable to examine a semi-enclosed domain such as the North Pacific Ocean using a regional model.

In the investigation of the anomalous state in the ocean, the anomalies can be considered as the perturbation quantities, though not necessarily very small, superimposed upon the basic long-term averages. In general, the oceanic anomalies are, at least to the lower order of approximation, generated by the atmospheric anomalies, such as the anomalous pressure, the anomalous wind, the anomalous heat-exchange and water flux (Namias,

1965). An approximate method for estimating the large-scale sea surface temperature anomalies due to atmospheric changes, proposed by Namias (1965) and extended by Arthur (1966) and Jacob (1967), has shown some degree of success.

One can also investigate the anomaly dynamics in the North Pacific Ocean by numerical simulation. The ocean model we developed for the anomaly study considers the actual configuration of the North Pacific Ocean and uses the complete dynamic equations with all large-scale physical processes taken into consideration, but is limited to constant depth. The basic numerical scheme used in the model is a modification of Haney's (1974) idealized ocean model. The space-staggered grid and the space-differencing scheme used in the present model follows that of the UCLA atmospheric general circulation model (Gates et al., 1971). In addition, the present model treats the upper boundary conditions in an improved manner. The heat flux between the ocean and the atmosphere is not only a function of the coupled air-sea temperatures but also a summation of all heating and interacting components calculated from empirical formulas for the heat balance at the naviface. In computing wind stress, the near-surface atmospheric stability is also taken into consideration. Both the longitudinal component and the meridional component of wind stress are used as boundary conditions in the momentum equations. Furthermore, since it is well known that salinity plays an important role in ocean dynamics at high latitudes, a prognostic equation for salinity conservation is also included in the hydrodynamic system.

Our study originated from the objective of NORPAX to understand the low-frequency fluctuations in the upper layer of the North Pacific Ocean and their relations to the overlying atmosphere. The major goal is to investigate the anomaly dynamics and to describe the configuration and evolution of the thermal anomalies in the North Pacific by numerical simulations. Because the anomalies are generally small, it is necessary to take a systematic step-by-step approach, from the spinup of an ocean model to the final anomaly experiments. This paper, the first of a series, describes the basic physics in the numerical model which is the basic tool for our thermal anomaly investigations, and shows the simulated long-term mean state in the North Pacific Ocean. Our major interest lies in the large-scale (>1000 km) and long-term (months to years) fluctuations in the North Pacific Ocean in relation to the overlying atmosphere. Follow-up papers will present the seasonal fluctuations in the North Pacific Ocean, and the dynamic mechanisms and results of anomaly experiments based on real-time specifications in the North Pacific model.

2. The dynamic model

The formulation of the model is based on the primitive equations expressed in a right-hand spherical coordinate system (λ, ϕ, z) on the surface of the earth with z taken positive upward from the mean sea level. The Navier-Stokes equations for incompressible and nonhomogeneous fluid with some basic physical approximations, namely, the Boussinesq approximation, the hydrostatic approximation and the eddy viscosity closure approximation, are integrated with time. We let (u,v) be the horizontal components of velocity $\mathbf{V}$ and define an advective flux operator as

$$\mathscr{L}(q) = a^{-1} \sec\phi[(uq)_\lambda + (vq \cos\phi)_\phi] + (wq)_z, \quad (1)$$

where q is any scalar quantity. With all symbols as defined in Table 1 and constants in Table 2, the governing equations are

TABLE 1. Description of symbols in ocean model.

t	time
λ	longitude
ϕ	latitude
z	elevation
Ω	angular speed of the earth
a	radius of the earth
g	acceleration of gravity
u	zonal component of the current
v	meridional component of the current
$\mathbf{V}$	horizontal velocity vector
w	vertical component of the current
T	temperature
S	salinity
ρ	density
F^λ	eastward frictional force per unit volume
F^ϕ	northward frictional force per unit volume
∇	horizontal gradient operator
$h(x)$	stepfunction ($h = 1$, $x \geqslant 0$; $h = 0$, $x < 0$)
G^λ	nonlinear component in the zonal direction
G^ϕ	nonlinear component in the meridional direction
Q_S	downward heat flux
Q_I	incoming solar radiation flux
Q_B	back radiation flux
Q_H	sensible heat flux
Q_E	latent heat flux
Q_0	incoming solar radiation flux with a clear sky
N_c	cloudiness in tenths
e_a	vapor pressure of air
e_s	saturated vapor pressure
T_s	ocean surface temperature
T_a	air temperature
c	Stefan-Boltzmann constant
L	latent heat of evaporation
ρ_a	air density
$\mathbf{V}_a$	wind velocity
q	specific humidity
P_a	air pressure
C_D, C_E, C_H	drag coefficient for momentum, latent heat and sensible heat, respectively
Ri	bulk Richardson number
τ^λ	longitudinal component of wind stress
τ^ϕ	latitudinal component of wind stress

TABLE 2. Parameters and constants in the ocean model.

Parameter of constant	Symbol	Value	Unit
Reference temperature	T_0	278.2	°C
Reference salinity	S_0	34.72	‰
Reference density	ρ_0	1.0276	gcm^{-3}
Thermal expansion coefficient	α	2.75×10^{-4}	K^{-1}
Saline contraction coefficient	γ	7.5×10^{-4}	(ppm)$^{-1}$
Longitudinal grid spacing	$\Delta\lambda$	2.5	deg
Latitudinal grid spacing	$\Delta\phi$	2.5	deg
Longitude at the western boundary	λ_0	varies	°W
Longitude at the eastern boundary	λ_i	varies	°E
Latitude of the northern boundary	ϕ_j	varies	°N
Total depth	D	4	km
Horizontal eddy viscosity	ν_1	2.5×10^8	cm^{2}s^{-1}
Horizontal eddy diffusivity	κ_1	2×10^7	cm^{2}s^{-1}
Vertical eddy viscosity	ν_2	1.5	cm^{2}s^{-1}
Vertical eddy diffusivity	κ_2	1	cm^{2}s^{-1}
Earth rotation rate	Ω	7.27×10^{-5}	s^{-1}
Specific heat of sea water	C_p	0.958	calg^{-1}K^{-1}
Time step	Δt	4.2	h
Ekman number	E	1.63×10^{-6}	nondimensional
Rossby number	Ro	2.03×10^{-5}	nondimensional
Reynolds number	Re	10	nondimensional
Péclét number	Pé	100	nondimensional
Lateral width of frictional boundary layer	L_F	1.2×10^{-2}	nondimensional
Lateral width of inertia boundary layer	L_I	4.5×10^{-3}	nondimensional
Drag coefficient under neutral state	$(C_D)_N$	2.5×10^{-3}	nondimensional
Constants in drag coefficients	b_1	52.9	nondimensional
Constants in drag coefficients	b_2	53.2	nondimensional
Constant in Richardson number	β_V, β_T	4.7	nondimensional
Reference height in Richardson number	Z_{10}	10^3	cm
Reference temperature in Richardson number	T_{v0}	290	K

$$u_t = \mathscr{L}(u) + v \sin\phi(2\Omega + a^{-1}u \sec\phi) \\ - (\rho_0 a)^{-1} \sec\phi p_\lambda + F^\lambda, \quad (2)$$

$$v_t = \mathscr{L}(v) - u \sin\phi(2\Omega + a^{-1}u \sec\phi) \\ - (\rho_0 a)^{-1} p_\phi + F^\phi, \quad (3)$$

$$p_z = -\rho g, \quad (4)$$

$$a^{-1} \sec\phi[u_\lambda + (v \cos\phi)_\phi] + w_z = 0, \quad (5)$$

$$T_t = \mathcal{L}(T) + Q, \tag{6}$$

$$S_t = \mathcal{L}(S) + H, \tag{7}$$

$$\rho = \rho_0[1 - \alpha(T - T_0) + \gamma(S - S_0)], \tag{8}$$

where all alphabetic subscripts denote partial derivatives and

$$F^\lambda = \nu_1[\nabla^2 u + a^{-2}(1 - \tan^2\phi)u$$
$$- 2a^{-2}\tan\phi \sin\phi v_\lambda] + \nu_2 u_{zz}, \tag{9}$$

$$F^\phi = \nu_1[\nabla^2 v + a^{-2}(1 - \tan^2\phi)v$$
$$+ 2a^{-2}\tan\phi \sin\phi u_\lambda] + \nu_2 v_{zz}, \tag{10}$$

$$Q = k_1\nabla^2 T + h^{-1}k_2 T_{zz}, \tag{11}$$

$$H = k_1\nabla^2 S + h^{-1}k_2 S_{zz}, \tag{12}$$

in which

$$\nabla^2(q) = a^{-2}\sec^2\phi q_{\lambda\lambda} + a^{-1}\sec\phi(a^{-1}\cos\phi q_\phi)_\phi. \tag{13}$$

Following Bryan (1969), the stepfunction $h(-\rho_z')$ in (11) and (12) incorporates the convective density adjustment mechanism in which $(-\rho_z')$ indicates the local lapse rate of density. At places where excessive upward heat flux occurs and where evaporation exceeds precipitation by a large amount, a layer of heavy cold and salty water will be formed in the upper layers of the ocean. Whenever the local lapse rate of density is less than the marginal vertical lapse rate (ϵ_ρ) which will ensure a marginally stable vertical density distribution, the hydrostatic instability exists in the adjacent layers. Since instability in the real ocean usually lasts for a short period of time, an instantaneous convective adjustment mechanism is activated in the model. Assuming the contribution to the density variation from the temperature and from the salinity are equally important, the marginally stable criteria for temperature and salinity can be estimated from ϵ_ρ and the coefficients for temperature and salinity expansions in the mean state of the ocean. Then, in case instability is detected between layers, the temperature, salinity and density in these vertical layers are mixed, respectively, into quasi-homogeneity.

The boundary conditions for the lateral and bottom solid boundaries are zero normal velocity, zero slip velocity and zero normal heat or salt flux on solid boundaries, i.e.,

$$u, v, T_n, S_n = 0, \tag{14}$$

where n denotes the normal derivative. On the equatorial southern boundary in addition to the no-normal velocity and no-normal fluxes of heat and salt, the tangential free-slip condition is also imposed, i.e.,

$$v, u_\phi, T_\phi, S_\phi = 0 \text{ at } \phi = 0. \tag{15}$$

At the bottom boundary $w = 0$ in addition to (14).

At the upper surface of the ocean, the "rigid-lid" approximation (Bryan, 1969) is employed in order to gain a more efficient time-dependent calculation. Other upper surface boundary conditions are

$$\nu_2(u_z, v_z) = \rho_0^{-1}(\tau^\lambda, \tau^\phi), \tag{16}$$

where τ^λ, τ^ϕ are the longitudinal and the latitudinal components of the surface stress;

$$\kappa_2 S_z = S_1(E - R), \tag{17}$$

where $E - R$ is the net difference of evaporation and precipitation and S_1 is the surface layer salinity; and

$$\kappa_2 T_z = Q_S/\rho_0 C, \tag{18}$$

where Q_S is the net downward heat flux across the atmosphere/ocean interface and C the specific heat of water at constant pressure. A detailed description of atmospheric forcing function, namely, the wind stresses and heating, is given in the next section.

The boundary conditions of zero normal flow, zero heat and salinity fluxes through the lateral boundaries, and zero vertical velocity at the balanced upper surface and at the bottom guarantee conservation of mass for the system as a whole and that supply of momentum and energy is limited to the sea surface.

Bottom topography and geothermal heat flux have been neglected at the lower boundary in this preliminary study. It is known that the bottom topography is important to the vertically integrated transport and can influence the path of the western boundary current in the ocean (Warren, 1963; Holland, 1967; O'Brien, 1971). However, we are more interested in the anomalous phenomena existing generally in the upper layer of the ocean where the baroclinic velocity field and seasonally varying heat contents may not be markedly affected by topography (Gill and Niiler, 1973).

There is no explicit wind-stirred mixed layer and no mesoscale eddy dynamics in the model. This is primarily because it is not known definitely whether there are significant effects for the aforementioned mechanisms to large-scale ocean circulations and to the gross estimations of the heat budget in the upper ocean, nor is there any simple *economical* method to incorporate these mechanisms into a relatively coarse-grid ocean model. Recent developments (e.g., Bryan et al., 1975; Holland and Lin, 1975; Robinson et al., 1977; Haney and Davies, 1976) have been devoted to improve these aspects in the ocean modeling.

a. The wind stress and the heat flux

The synoptic net downward heat flux, according to the heat balance equation at the naviface, can be written as

$$Q_S = Q_I - Q_B - Q_H - Q_E, \qquad (19)$$

where Q_I is the net downward flux of solar insolation and Q_B, Q_H, Q_E are upward fluxes of infrared radiation, sensible heat and latent heat, respectively, as defined in Table 1. Table 1 also defines all other notations used in the following formulas.

The solar radiation flux can be calculated from a simplified formula with empirical constants obtained from atmospheric climatology (Johnson et al., 1958; London, 1957; Vonder Haar and Hanson, 1969) as

$$Q_I = 0.95Q_0(0.74 - 0.6N_c). \qquad (20)$$

The net upward infrared heat flux is calculated from

$$Q_B = 0.985cT_S^4(0.39 - 0.06e_a^{1/2})(1 - 0.6N_c^2), \qquad (21)$$

and the sensible and latent heat are computed from

$$Q_H = \rho_a C_H C_p |V_a|(T_s - T_a), \qquad (22)$$

$$Q_L = \rho_a C_E L |V_a|(q_s - q_a), \qquad (23)$$

where $|V_a|$ is the wind speed at 10 m above the surface. Since most observations are in vapor pressures, humidity is related to the vapor pressure by

$$q = 0.622e/P_a, \qquad (24)$$

where P_a is the mean atmospheric surface pressure. The saturated vapor pressure at the ocean surface temperature can be calculated from the Clausius-Clapeyron equation (Hess, 1959), i.e.,

$$\log_{10}e_s = (9.4051 - 2353/T_s). \qquad (25)$$

The momentum flux at the ocean/atmosphere interface is expressed as the surface wind stresses,

$$(\tau^\lambda, \tau^\phi) = \rho_a C_d |V_a|(u_a, v_a), \qquad (26)$$

where (u_a, v_a) are components of V_a. Following Deardorff (1968) and using data of Businger et al. (1971), the exchange coefficients of heat, water and momentum are taken as functions of atmospheric stability:

$$\left.\begin{array}{l} C_D = (C_D)_N \exp(-2\beta_v\mathrm{Ri}) \\ C_H = C_E = (C_H)_N \exp[-(\beta_v + \beta_T)\mathrm{Ri}] \end{array}\right\} \begin{array}{l} \text{for stable cases} \\ \quad (\mathrm{Ri} > 0) \end{array} \qquad (27a)$$

$$\left.\begin{array}{l} C_D = (C_D)_N\left[1 + \dfrac{7}{b_1}\ln(1 - b_1\mathrm{Ri})\right] \\[2ex] C_H = C_E = (C_H)_N\left[1 + \dfrac{11}{b_2}\ln(1 - b_2\mathrm{Ri})\right] \end{array}\right\} \begin{array}{l} \text{for unstable cases} \\ \quad (\mathrm{Ri} < 0) \end{array} \qquad (27b)$$

where the bulk Richardson number

$$\mathrm{Ri} = \frac{gZ_{10}}{T_{vo}V_a^2}\left[(T_a - T_s) + 0.38T_a\frac{e_a - e_s}{P_a}\right], \qquad (28)$$

and β_v, β_T, $(C_D)_N$, b_1, b_2, Z_{10} and T_{vo} are constants (Businger et al., 1971) are listed in Table 2. The coefficient of water particle exchange is assumed to be the same as that of the exchange of heat. All values of atmospheric parameters for the annual mean forcing are the 20-year (1950–70) long-term mean data provided by the (on magnetic tapes) National Marine Fishery Service, La Jolla. This mean wind field data do not differ significantly from those of Hellerman (1967). The evaporation and precipitation data $(E - R)$ for the boundary condition of the salinity prediction are obtained from Jacob (1951).

b. The hydrostatic equation

The equation of state defines the density in terms of temperature, salinity and pressure. The departure of pressure at any level in the ocean from the vertically averaged pressure is uniquely determined by the density as

$$p'(z) = \int_z^0 \rho g dz - D^{-1}\int_{-D}^0\left(\int_z^0 \rho g d\xi\right)dz. \qquad (29)$$

c. The vorticity equation

The exclusion of kinematic surface variations makes the surface pressure impossible to calculate in a prognostic sense. Instead we compute the shear velocity components (u', v') as prognostic variables with the pressure terms substituted by the hydrostatic equation. The vertical mean velocity $(\hat{u}, \hat{v})$ is obtained from the streamfunction by solving the vorticity equation. Then, the total velocity is the combination of the vertical mean velocity and the deviation from the vertical mean, i.e.,

$$(u, v) = (\hat{u} + u', \hat{v} + v'). \qquad (30)$$

The surface and bottom boundary conditions on w permit us to define the nondivergent vertically integrated streamfunction which satisfies the integrated continuity equation, i.e.,

$$\hat{u} = -a^{-1}\psi_\phi, \qquad (31)$$

$$\hat{v} = a^{-1}\sec\phi\psi_\lambda, \qquad (32)$$

where, for any scalar q,

$$(\hat{q}) = D^{-1}\int_{-D}^0 (q)dz \qquad (33)$$

is the vertically integrated mean. The predictive

vorticity equation can be obtained by eliminating pressure terms in (2) and (3):

$$\nabla^2 \psi_t = a^{-1} \sec\phi\{(\hat{G}^\phi + \hat{F}^\phi)_\lambda$$
$$- [(\hat{G}^\lambda + \hat{F}^\lambda) \cos\phi]_\phi\} - a^{-2} \sec\phi f_\phi \psi_\lambda, \quad (34)$$

where f is the Coriolis parameter and

$$G^\lambda = \mathscr{L}(u) + (uv/a) \tan\phi, \quad (35)$$

$$G^\phi = \mathscr{L}(v) - (uv/a) \tan\phi. \quad (36)$$

The predictive equations for the vertical shear current (u',v') are (2) and (3) subtracting their respective vertical means. The temperature (T) and salinity (S) are predicted from (6) and (7). The diagnostic variables are w, ρ, p obtaining from (5), (8) and (29), respectively.

3. Finite-difference equations

It is vitally important that certain integral constraints such as the conservation of total mass and total energy during adiabatic and nondissipative processes are assured. In the construction of the model, we have used the quadratic conserving method (Arakawa, 1966; Bryan, 1969) to assure that the above integral constraints are satisfied.

In the NORPAX model, the actual configuration of the North Pacific Ocean is taken into account by approximating the coastline with meridians or latitude circles passing through the nearest grid points as shown in Fig. 1. The origin of the coordinates is taken at the intersection of the mean sea surface, the equator, and the western boundary of the ocean $(\lambda_0 = 120°E)$. The whole North Pacific domain is from 120°E to 80°W in longitude and from 0°N to 65°N in latitude with 2.5° grid spacing in both horizontal directions. The vertical coordinate z is set for 10 variable-thickness layers at depths of 10, 30, 60, 100, 150, 225, 350, 700, 1500 and 3000 m below the surface with a maximum depth of 4000 m. It is obvious that such emphasis has been put on the column of water above the permanent thermocline.

There are five prognostic variables (u',v',ψ,T,S) and three diagnostic variables $(w, \rho$ and $p)$ in the model. To be consistent with the requirements for integral constraints, the space-staggered grids are arranged in such manner that T, S and ρ are basically computed at the integral grid points (i,j,k); u,v at the half-integer points $(i + ½, j + ½, k)$; and w at the $(i, j, k ± ½)$ point. The streamfunction ψ is two-dimensional and is computed at the (i,j) points.

In the finite-difference equations, the adopted numerical scheme is that of Haney (1974), based on Arakawa (1966). The center-difference scheme is extensively used in both the spatial and the temporal differences. However, in order to suppress the computational mode in the long-term integration by using the leapfrog scheme (Lilly, 1965), the Euler-Matsuno scheme is periodically employed every 25 time steps (Matsuno, 1966). The Coriolis term is
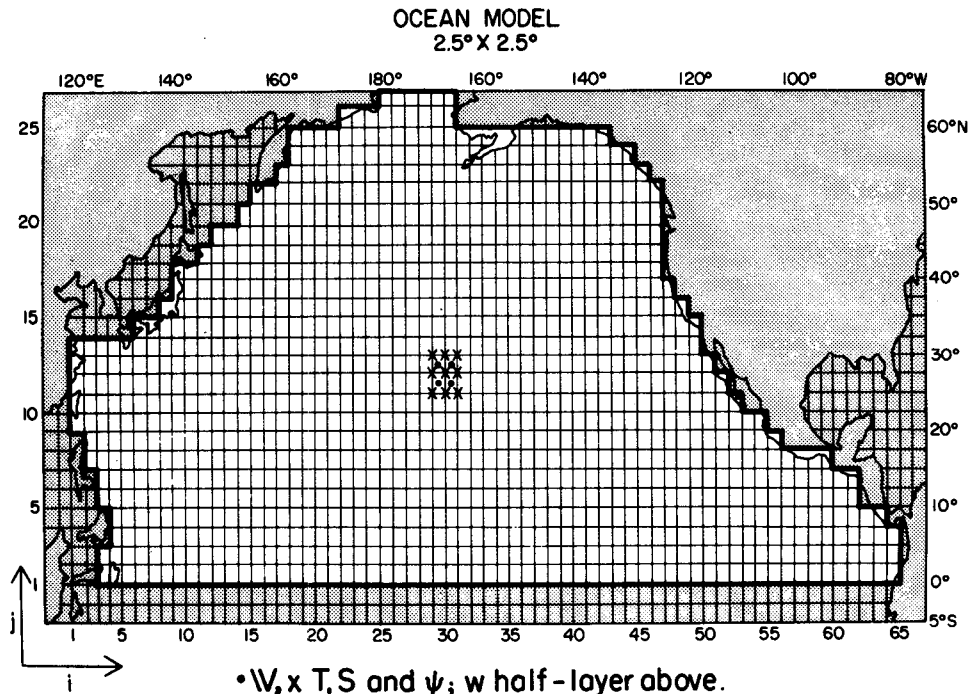
OCEAN MODEL
2.5° X 2.5°

$\cdot$ W, x T,S and ψ_j w half-layer above.

FIG. 1. NORPAX model 2.5° × 2.5° grid mesh and parameter computing points: x temperature and salinity points, ● velocity points.

treated implicitly, with a slight damping, which permits a time step longer than the inertial period. Details for the finite-different equations in divergence form can be found in Huang (1973); the sequence of computations and major software for the model are documented in Huang *et al.* (1977).

4. Results

a. Three stages of integration

The initial condition for the first phase is a stable pattern of mean temperature and salinity with no currents. The model with 5° in horizontal spacing and seven vertical layers was integrated for more than 40 years using 8 h time steps until a quasi-equilibrium state was reached. After 10 years of integration, the local rate of change term was everywhere much smaller than other major terms in both the momentum and the thermohaline balance equations, as will be shown later. The results of the model output after 40 years of integration were interpolated to 2.5° and 10 layers to be used as initial conditions for the second phase of the model. Parameters used in the 2.5° version of the model are summarized in Table 2. Note that the horizontal viscosity used is 2.5×10^8 cm^2 s^{-1} and the diffusivity is about an order of magnitude smaller. The vertical viscosity used is 1.5 cm^2 s^{-1}. This version of the model was then integrated for more than 20

years with time steps of 4.3 h until another quasi-equilibrium state was reached. Then the seasonally varying, time-dependent atmospheric conditions were imposed as upper boundary forcing conditions. The integration was carried out for another 20 years. The last year's output was considered as the long-term, seasonally varying state in the North Pacific Ocean. The present paper presents the long-term annual mean state. In the follow-up papers (II and III), we will describe in detail the time-dependent seasonal variability and the anomaly experiments.

b. Energetic analysis under quasi-equilibrium state

For each individual computational subvolume, balances of mass, momentum, heat and water were evaluated in the model. Fig. 2 shows the local balance of all major physical processes included in the equations of motion, namely, the Coriolis term, the pressure gradient term, the horizontal and vertical viscous terms, and the horizontal and vertical nonlinear terms for a subvolume near the equator. Values indicating the relative magnitudes of each term in the momentum equation have been normalized in such a manner that the absolute sum of all terms is 100%. A set of such analyses for three time steps, each separated from the other by 10 days, in the last 30 days of integrations at this stage, were performed and the results show no
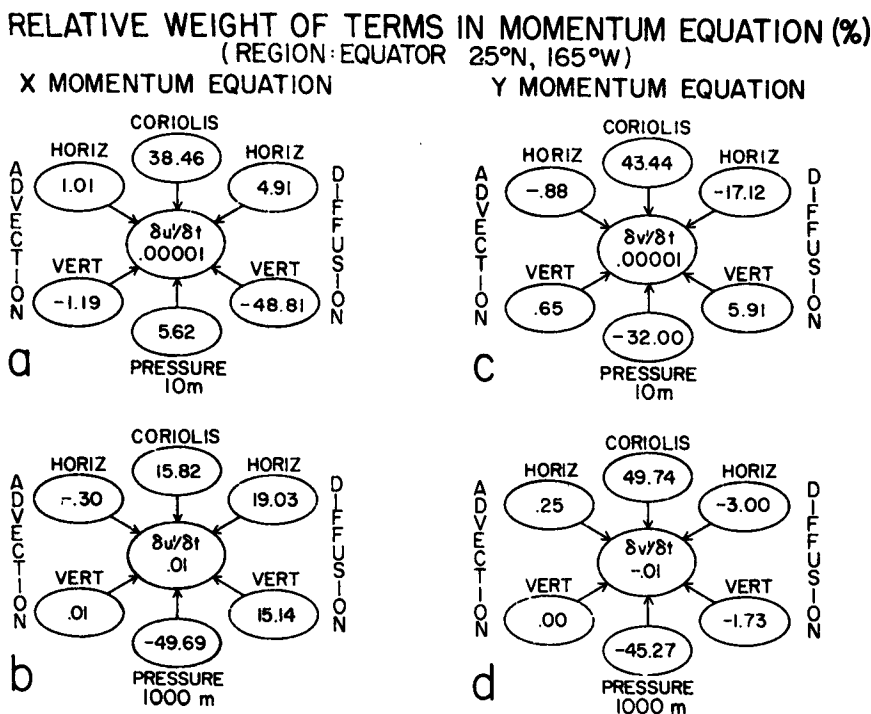

FIG. 2. Relative weight of terms (%) for the momentum equation in the equatorial regions: (a) and (b) the *x* component of momentum balance for the layers near 10 and 1000 m depths; (c) and (d) the *y* component of momentum at the same depths.

noticeable differences one from another. This indicates that the model has reached a quasi-equilibrium state.

As shown in Fig. 2a, major forces are in near Ekman-geostrophic balance in the surface layer and in near geostrophic balance below. In the x component of momentum equation, the pressure gradient force, which is rather moderate in the longitudinal direction along the equator, works together with the Coriolis force to balance the x component of the surface wind stress, which is quite strong because of the trade wind. The horizontal diffusion of momentum as well as the nonlinear effect are also important in the equatorial region. The y component of Coriolis force is considerably larger than the x component because the equatorial currents flow mostly in an east-west direction. The north-south density gradient is larger than that in the east-west direction while the meridional component of the trades is much weaker than the zonal component. The balance of the y component is maintained between the Coriolis force, working together with the meridional wind stress and the pressure gradient force, assisted by the strong viscous effect.

In the lower layers, the x component of the viscous force becomes important due mostly to large vertical and meridional shear. The viscous force together with the Coriolis force balance the east-west pressure gradient force. The y component of momentum in the lower layers is generally in geostrophic balance as shown in Fig. 2d. In the mid-

latitude open ocean about 2000 km northwest of Hawaii in the Pacific wind drift current region, Ekman dynamics are dominating in the x component while the Ekman-geostrophic balance is maintained in the y component of momentum equations (figures not shown). At the depth of the intermediate water, there is essentially a geostrophic balance with most other processes being negligibly small. In the Kuroshio region, the surface current also maintains an Ekman-geostrophic balance in the x component and in near geostrophic balance with higher frictions in the y component of the momentum equations (figures not shown). Similarly, a geostrophic balance is shown in the deep layers. In summary, below the surface layers geostrophy is the dominating balance in the present model, while the Ekman drift together with associated convergence and divergence play an important role in the dynamic balance of the surface layer. The nonlinear effect is small in most of the ocean away from boundaries but is not negligibly small in the equatorial and in the western boundary regions.

A similar analysis of the various terms in the temperature and salinity equations is shown in Fig. 3 for two depths in a subvolume near the equator (and at 170°W). The quantities, indicated in this figure as horizontal and vertical advection, are the terms $\nabla \cdot (\mathbf{V} \phi)$ and $\partial/\partial z(w\phi)$, respectively, where ϕ is S or T. As shown, these terms taken individually dominate over the diffusion, although the terms collectively balance the diffusion terms. This is ad-

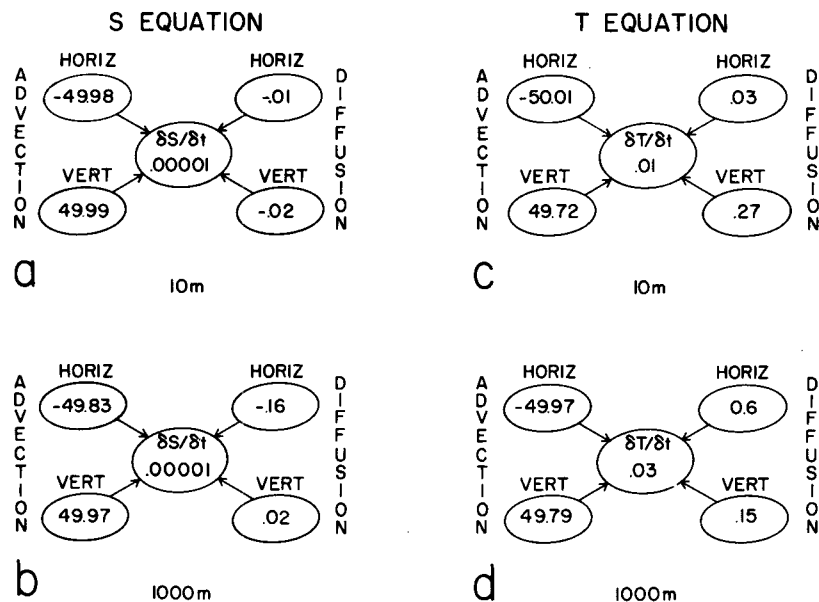## RELATIVE WEIGHT OF TERMS (%) (Equatorial Region. 0°N, 165°W)

FIG. 3. As in Fig. 2 except for density balance near equatorial region: (a) and (b) for the salinity equation for layers near 10 and 1000 m depths; (c) and (d) same as (a) and (b) except for temperature equation.

mittedly deceptive since if one splits the term $\mathbf{V}\cdot(\mathbf{V}\phi)$ into $\mathbf{V}\cdot\mathbf{V}\phi$ and $\phi\mathbf{V}\cdot\mathbf{V}$, with a similar split of $\partial/\partial z(w\phi)$, it is found that $\phi\mathbf{V}\cdot\mathbf{V}$ dominates over $\mathbf{V}\cdot\mathbf{V}\phi$ and $\phi\partial w/\partial z$ over $w\partial\phi/\partial z$. Yet the terms $\phi\mathbf{V}\cdot\mathbf{V} + \phi\partial w/\partial z$ taken together must vanish as required by the incompressibility constraint. This general tendency holds true for the entire ocean regardless of where the computational subvolume is. In considering the total balance, the surface heating turns out to be as important as the advection. The former may even be more important than the latter in the open-ocean region where the current is relatively weak.

The above discussion points up a problem for those who are seriously attempting to make *in situ* measurements of heat fluxes in certain areas of the ocean. Since the dominating influence in the local thermal energy equation is the surface heating from the atmosphere and the difference of two large advective flux terms, small errors in measurements, especially in the vertical flux of heat, will lead to a great uncertainty in the heat budget study.

c. Annual long-term mean state

In the following paragraphs, results of the NOR-PAX ocean model under the annual long-term mean atmospheric forcing are presented. In addition, certain comparisons between the simulated annual mean state and the observational data in the North Pacific Ocean are discussed. Note that all meteorological and oceanographic observations deal with time-dependent phenomena. The seasonal cycle in nature has unequivocally dominated the major low-frequency fluctuations in the ocean and atmosphere. The winter and the summer pattern of physical parameters such as currents and temperatures are two extreme characteristic regimes in the annual cycle. Most long-term mean observational data are grouped, analyzed and presented in monthly or seasonal mean patterns. It is therefore necessary to point out that precise comparisons between the simulated long-term mean state and the observational data are not always practical. Therefore, while emphasis is on the approximate similarity between the simulated results and the observed values, one must occasionally use the long-term mean winter or summer patterns, the only ones available, to demonstrate the agreement in gross features between the simulations and the observations.

d. Mass transport streamfunction

Fig. 4 shows the contour plot of the mass transport streamfunction in a nearly equilibrium state under annual mean surface wind stresses and heating after more than 60 years of integration. Three large-scale gyral circulations are well developed, similar

to the Munk solution (Munk, 1950). The anticyclonic subtropic gyre is quite realistically portrayed and the western intensification of the boundary current is clearly demonstrated. The major part of the mid-latitude west drift current constitutes the northern portion of the subtropic gyre. The California Current, the North Equatorial Current and the Western Boundary Current are all included in this gyral current system. The maximum total transport in the Kuroshio region near Japan reaches 56×10^6 m^3 s^{-1} which agrees quantitatively with observed mean transport in the area (Nitani, 1972). Two cyclonic gyres are also well simulated, one of which is in the subarctic region, the other in the tropic region. The subarctic cyclonic gyre consists of the west drift current, the Alaskan Current, the Aleutian Current (together with its extension through the Bering Sea), the Kamchatka Current and the Oyashio Current. The mass transport of the model output in the Kamchatka Current region has a southward transport of 21×10^6 m^3 s^{-1} and in the Oyashio region, about 2×10^6 m^3 s^{-1}. Reid's (1973) analysis of the Boreas data indicates a geostrophic transport across 55°N relative to 1500 db of 23×10^6 m^3 s^{-1} in winter, while calculations made from summer data indicate only 8×10^6 m^3 s^{-1} (Allen, 1964). In the Oyashio region, Hata's (1965) data show a southward transport across 43°N of about 3×10^6 m^3 s^{-1} in winter and about 2×10^6 m^3 s^{-1} in spring and summer. The model output agrees satisfactorily with observed data. However, the simplification of configurations in the model has ignored the existence of islands, including the Aleutian chain of islands, which results in the disappearance of many interesting small-scale features in the circulation pattern. We notice that the Aleutian stream is absent in the streamfunction and the Alaskan gyre is flowing to the west rather than the southwest. The mass transport in the tropic cyclonic gyre with the annual mean atmospheric forcing reaches a maximum value of 25×10^6 m^3 s^{-1}. The gross feature of the streamfunction patterns shows a distribution similar to that of the wind stress curl. Transports in the boundary regions between the cyclonic and the anticyclonic gyral circulations are weak, in coincidence with the latitude of zero curl regions, and the maximum transport occur at corresponding maximum wind stress curl latitudes as pointed out by Munk (1950). The barotropic current deduced from the streamfunction is generally small, less than 1 cm s^{-1} everywhere in the basin except in the western boundary region.

Note that comparisons between the observed transports and the simulated transports are meaningful only in a relative sense for the gross feature. The major difficulty lies in the levels of no motion used for individual observations in approximating the transport. The simulated transports of the model
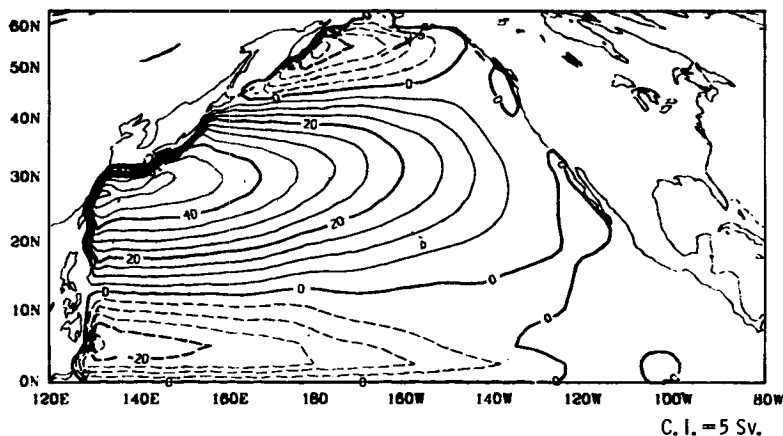
FIG. 4. Contour plot of mass transport streamfunction at contour interval 5×10^6 m^3 s^{-1}.

fall within the range of observations, while the simulated velocity of currents are generally lower than observations, as we will see in the next section. In a viscous coarse grid model, the velocity is expected to be weak. However, the deep depths along the coastal region implied in a constant-depth model may compensate for some of the ignored bottom effect, which is known to strengthen the boundary transport. This may help explain why the simulated values are close to the observed values. The viscosity used in the present simulation is still too small for the grid separations as indicated in the slightly wavy streamlines in the midlatitude region near Japan as shown in Fig. 4 (Takano, 1975). The low viscosity may also help in building up the transport in the model ocean, especially along the western boundary.

e. Velocity patterns

Fig. 5 shows current vector streamline plots for 10, 250 and 2500 m, depths. In the surface layer the
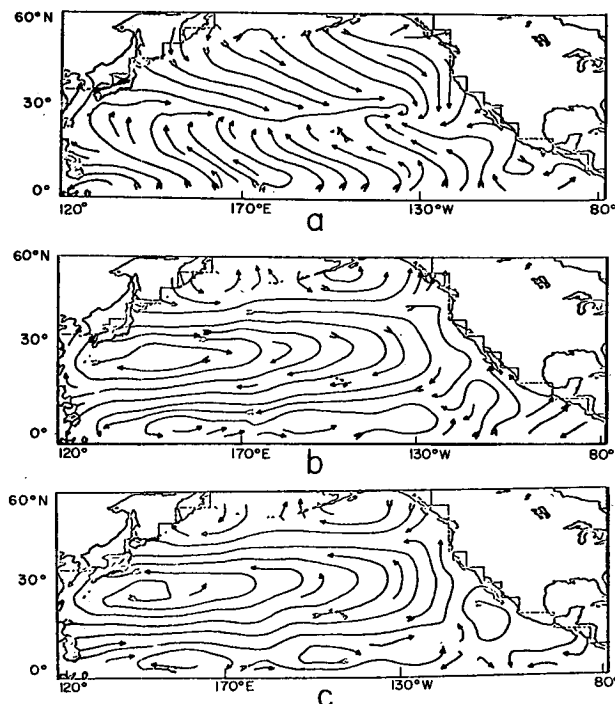
FIG. 5. Current vector streamline plots: (a) at 10 m depth; (b) at 225 m depth; (c) at 1500 m depth.

major swift currents occur in the equatorial region as well as in the western boundary region. The maximum current occurs in the eastern central Pacific near the equator with a speed of 95 cm s^{-1}. The Kuroshio Current only reaches 64 cm s^{-1} due mostly to the coarse-grid meshes. The western boundary current is only barely resolved at the horizontal separation of about 175 km. The non-dimensional length scale L_F for a frictional western boundary is proportional to the one-third power of the Ekman number (E $= \nu_1/2\Omega a^2$ and $L_F = $ E$^{1/3}$). The value of L_F for the second phase is 0.012. The resolvable length scale for the Kuroshio Current is 340 km during the second stage of computations. It is obvious that the grid separation is just barely comparable with the observational width of the western boundary current. Thus, the coarse-grid separations have led to smaller current values than the observations, while the transport values are comparable. The scale width L_I of the inertial boundary layer is proportional to the square root of the Rossby number ($L_I = $ Ro$^{1/2}$). The nonlinear effects were included in the model with $L_I = $ 0.0045. After comparing L_F with L_I, it is evident that while the inertial effects are smaller than the viscous effects, they are not negligible, as ascertained in the previous momentum analyses. The surface currents in the tropics are generally flowing westward. The Equatorial Countercurrent is not clearly shown, most probably due to the coarse grid.[2] The Oyashio merges into the extension of the Kuroshio to form the North Pacific drifting current. It is evident that the surface current is dominated by the Ekman wind-induced flow with deflection to the right of the wind pattern as shown in Fig. 5a. In the equatorial region, the flow pattern splits into a northward branch to form the Kuroshio and a southward branch to the equatorial current system near the Phillipine Sea. The existence of the subarctic convergence zone is clearly shown along the mean track of the Kuroshio and Oyashio merging zone off the western boundary at about 40°N, leaning southward to the eastern North Pacific at about 35°N. A mesoscale anticyclonic eddy, recognized as the Eastern Gyral by Sverdrup (Sverdrup et al., 1942), exists in the midlatitude eastern North Pacific. Fig. 5b shows the current vector streamline plot at 250 m depth. Notice that the current near the equatorial region is flowing eastward, representing the combined flow of the North Equatorial Countercurrent and the Undercurrent. The Kuroshio is well developed and has maximum velocity of 35 cm s^1, the highest value in the layer. The 250 m gyre picture looks very much like transport maps of White (1975). Note that the surface convergence line shown in

Fig. 5a occurs over the center of the geostrophic gyre at 250 m and that the eastern surface gyre does not show up at depth. The Kuroshio Current, the west wind drift, the California Current and the North Equatorial Current are predominently and easily identified with the anticyclonic gyre. The tropic cyclonic gyre consisting of the North Equatorial Current, the Equatorial Countercurrent together with the Equatorial Undercurrent, is clearly demonstrated. Other less obvious currents, such as the Oyashio and the Alaska Currents, are indicated in the circulation pattern. Figs. 5a and 5b simulate the gross nature of the circulation patterns in the upper layers of the North Pacific Ocean while Fig. 6 presents the observed surface mean current in more detail. The simulated current near 700 m is rather weak and the circulation indicates a different pattern (figure not shown). In the deep layers currents are slightly stronger than in layer 7 and the circulation pattern below the depth of 1500 m, as shown in Fig. 5c, flows opposite to that of the upper layers. The current beneath the Kuroshio is flowing southward at a much slower speed of 4 cm s^{-1} and there is clearly a weak cyclonic circulation in the subtropic region. Deep water is slowly flowing southward from high latitudes in the western North Pacific and northward in the eastern North Pacific, which generally agrees with the deep circulation pattern deduced from the geostrophic calculation by J. L. Reid (1976, personal communication).

Fig. 7 shows the vertical velocity contours at depths of 20, 300 and 2200 m in the model ocean. The solid contour indicates upwelling and the dotted line, downwelling. There is, in general, strong upwelling along the equator, especially in the eastern part of the midtropic region where the maximum upwelling reaches 5 m day^{-1}. Upwelling at the mid-latitude, western boundary region is relatively weak in the surface layer. Weak upwelling also exists along the California coast. Weak downwelling exists in most subtropical and eastern tropical regions away from the equator. This pattern of equatorial upwelling and subtropic downwelling extends to a depth of more than 700 m. In deeper layers, upwelling along the western boundary and downwelling in high latitudes and in the northwestern part of the North Pacific become even stronger at the depth of 1500 m. The maximum upwelling reached 3.5 m day^{-1} in the western boundary at a depth of 200 m and a maximum downwelling of approximately 1 m day^{-1} at the high-latitude region occurred at a depth of 550 m. The equatorial upwelling decreases below 200 m and a slight upwelling is indicated in the tropics at 1000 m depth. However, below 1000 m, the general trend of upwelling and downwelling generally changes signs. There exist moderate downwelling in the western boundary at 1000 m and weak upwelling in high lati-

---

[2] It was found later that this is also due mainly to the automatic elimination of half of the data points during plotting.
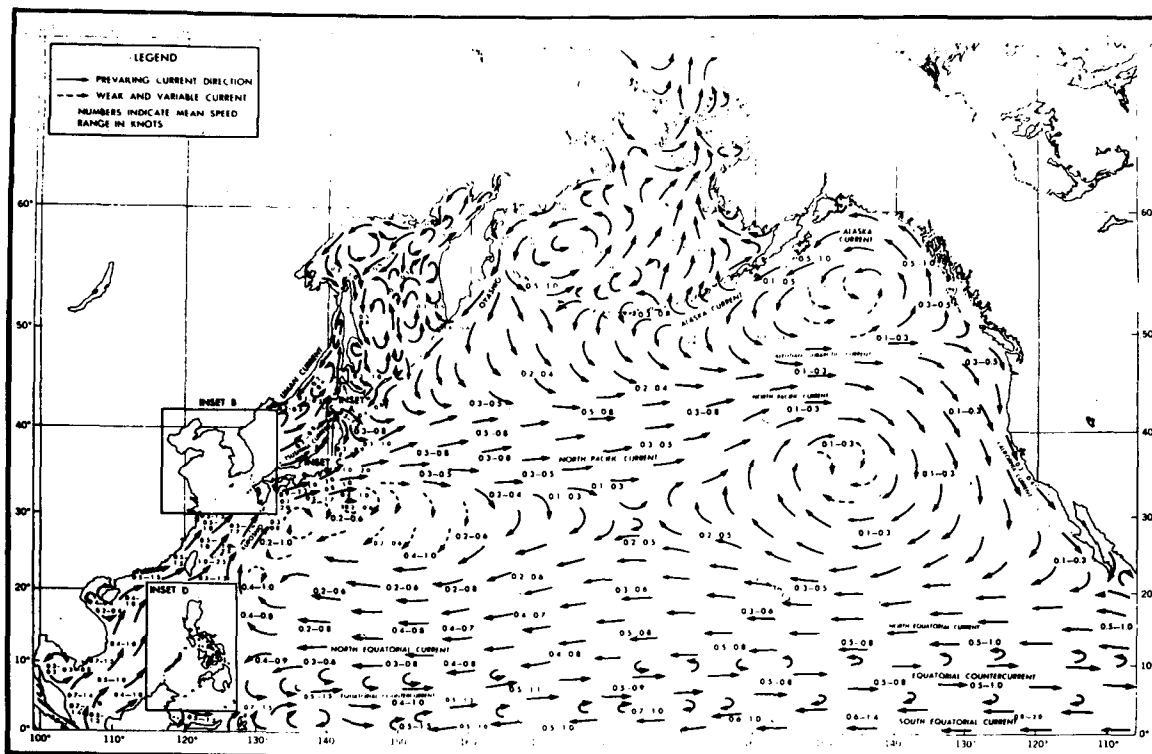
a
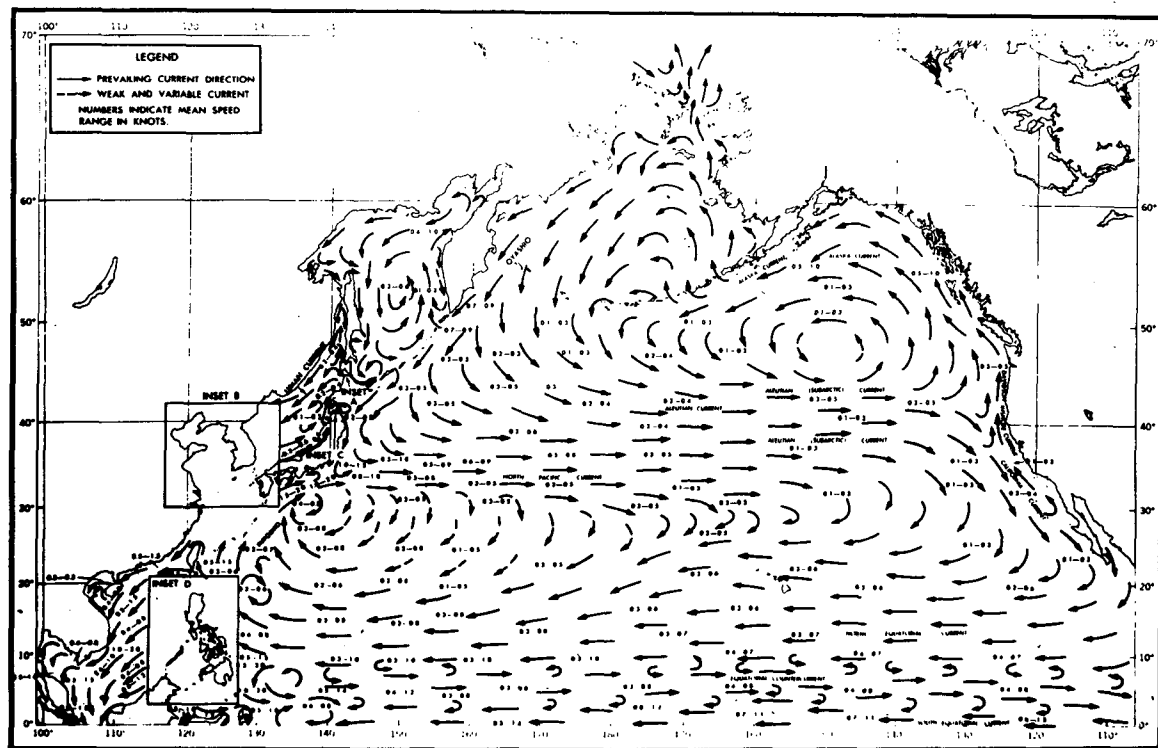
b

FIG. 6. Observed surface mean current pattern in the North Pacific Ocean (from U. S. Department of Commerce, 1961): (a) summer; (b) winter.

tudes. At the depth of 2500 m, weak upwelling becomes evident in most of the northern boundaries and moderate downwelling exists in the equatorial region. There is weak but broad upwelling in the interior of the tropics. From the previous figures we notice that major large-scale features in the model match reasonably well with observed mean current patterns and inferred upwelling distributions in the North Pacific Ocean.

f. Temperature and salinity fields

Fig. 8 shows the simulated temperature patterns at depths of 10, 250 and 3000 m. The surface temperature distribution (Fig. 8a) shows an equatorial cool region extending from the east boundary to 180°, corresponding to the equatorial upwelling region. The broadest cold water extends to 5°N with a minimum of 23°C at the equator. There is a broad
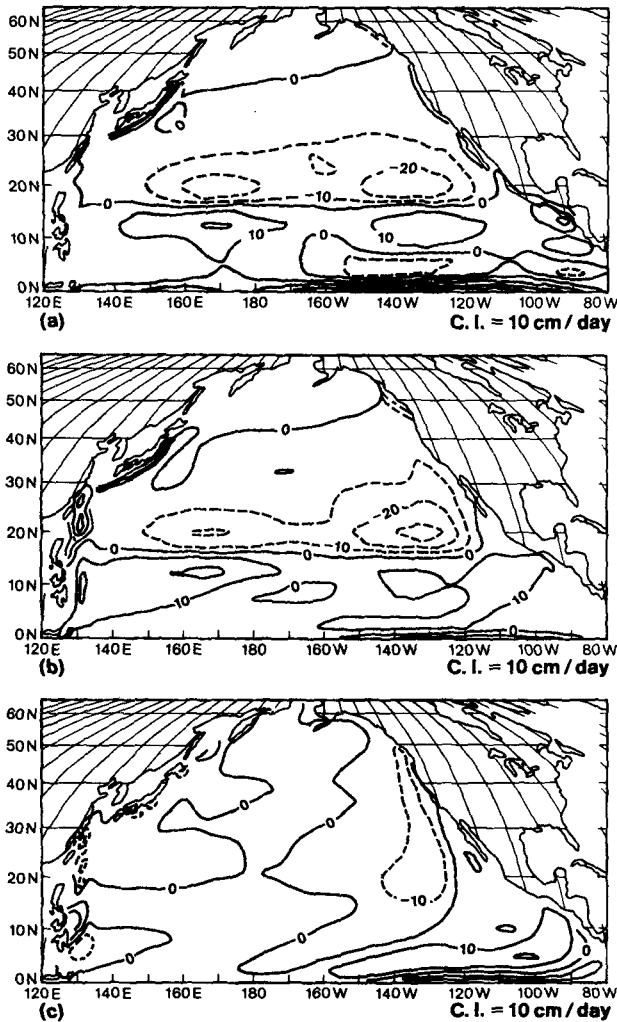
FIG. 7. Simulated vertical velocity contours at different levels in the North Pacific Ocean: (a) at 20 m depth; (b) at 300 m depth; (c) at 2250 m depth.
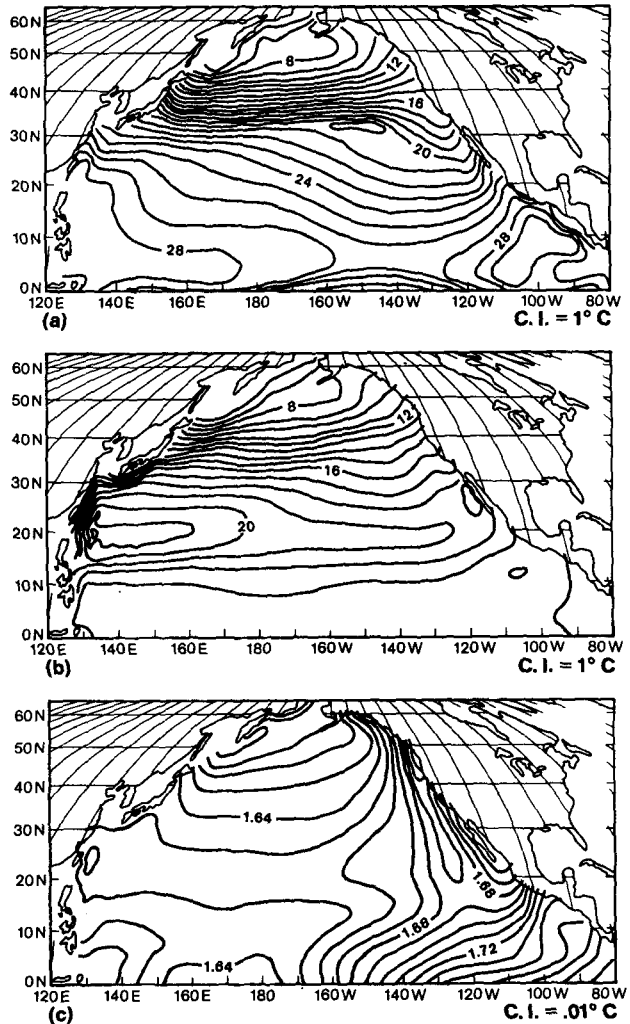
FIG. 8. Simulated temperature distribution (°C) at different layers: (a) 10 m; (b) 225 m; (c) 3000 m.

warm water region in the western tropic and a narrow one near the eastern boundary north of the equator. A sharp meridional temperature gradient exists at midlatitude off the western boundary along 35°N. The upwelling along the equator does not penetrate deeply around 300 m, warm water masses in the western and eastern tropics can still clearly be discerned, and a sharp temperature gradient along the western boundary develops. At 1000 m (figure not shown), the temperature is quasi-homogeneous and is slightly warmer in the south. The deep water temperature at 3000 m shown in Fig. 8c indicates a nearly spatial homogeneity with a slight cooling in the north. In general, the simulated surface temperature distribution agrees well in gross features with the mean sea surface temperature pattern in the North Pacific Ocean as shown in Fig. 9 (Masuzawa, 1972). In the midlatitudes and tropics, the agreement between Figs. 8a and 9 is very good.
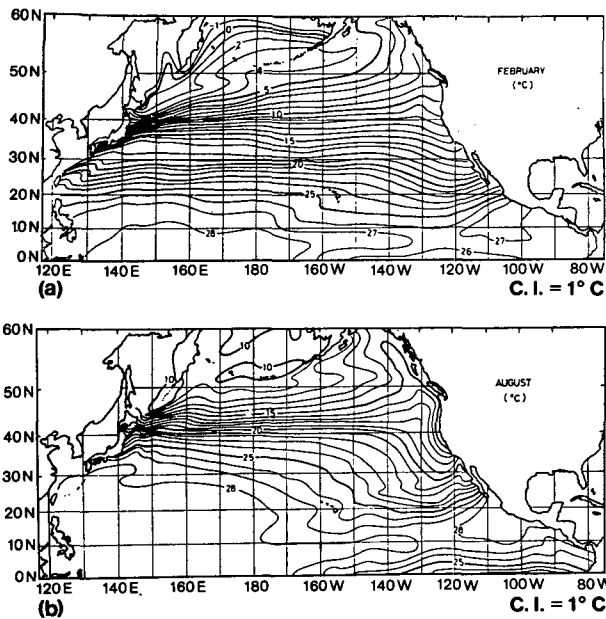
(a)

C. I. = 1° C

(b)

C. I. = 1° C

FIG. 9. Observed surface temperature distribution (°C) in the North Pacific Ocean (from Masuzawa, 1972): (a) summer; (b) winter.

However, a close examination reveals that the observed winter temperature at high latitudes is slightly lower than the model temperature, which is much closer to the summer values (Fig. 9a). The annual mean atmospheric data used in the model as upper boundary conditions are probably biased to summer conditions mostly because there were more observations during the summer season. Similar temperature patterns extend to below 100 m with a slight overall decrease of about 2°C at 60 m and about 7°C at 100 m, except for the cool water along the equator, that has been narrowed to 1° or 2° in latitude at 60 m and disappeared at 100 m.

Simulated temperature distributions for longitudinal vertical cross sections at 5, 15, 25 and 35°N are shown in Fig. 10. There is always a sharp vertical temperature gradient of about 0.5°C m^{-1} simulating the main thermocline, which is about 300 m in the tropics. The gradient is about 0.015°C m^{-1} in the intermediate water from the main thermocline down to the depth of 1000 m. At greater depths the temperature is rather homogeneous with a weak vertical gradient about 0.0007°C m^{-1}. Water is generally warm in the west North Pacific (28–29°C),
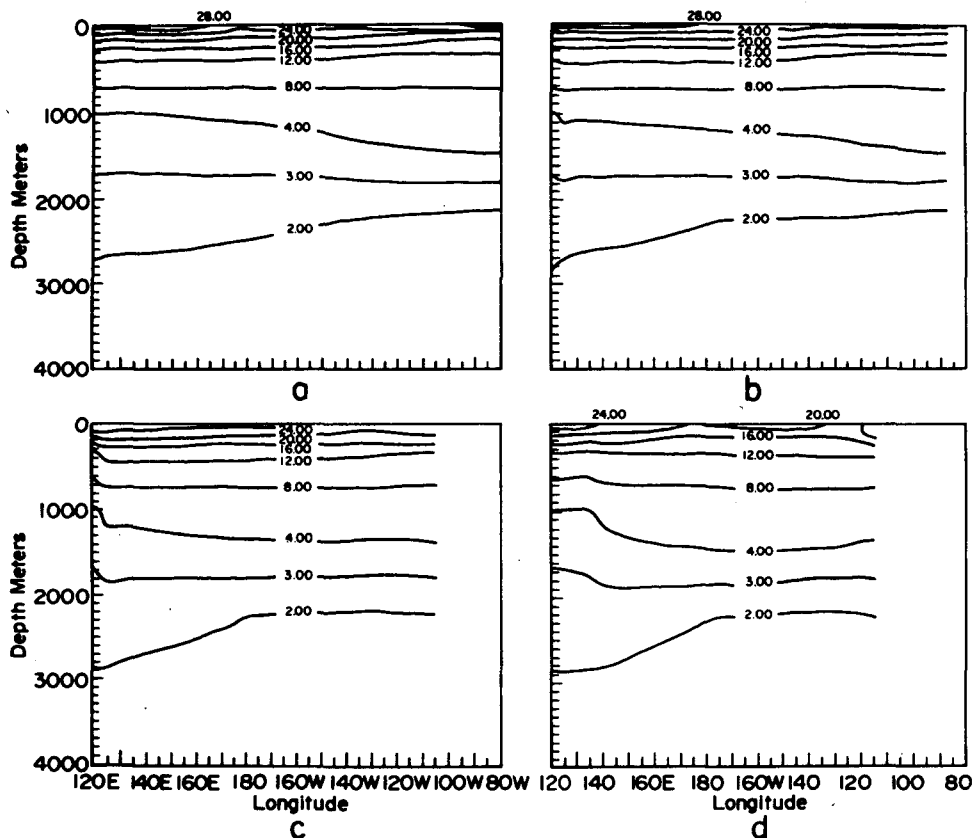
FIG. 10. Simulated temperature (°C) profiles in east-west vertical cross sections: (a) 5°N latitude; (b) 15°N latitude; (c) 25°N latitude; (d) 35°N latitude.

cool in the middle-east North Pacific (~24–25°C), and becomes warm again near the eastern boundary (~28–29°C) in the surface layer at 5°N near the tropics. The eastern warm mass extends westward to 135°N and more. The homogeneity of the upper layer implies that the surface mixed layer is about 50–100 m deep in midlatitudes as shown in Fig. 10d. The observed temperature distributions corresponding to the longitudinal cross sections of Fig. 10 are shown in Fig. 11, obtained from Muromtsev (1963) and from Masuzawa (1972). The general features of the model output agree qualitatively with the observed data. The same order of magnitude of vertical temperature gradients exists in the upper 350 m. However, there are no undulating distributions of temperature and no double thermoclines in the simulated temperature field as occur in the observed data. This is probably due to coarse vertical separations in the model. The model of the eastern North Pacific produced more warm water in middle latitudes, where the isotherms rise very gently to the east in the intermediate water depth (300–700 m), as indicated in Figs. 10c and 10d, than that in the Muromtzev (1963) atlas where the isotherms rise

rather sharply toward the east as shown in Figs. 11c and 11d.

Four meridional cross sections of temperature distribution from the model output are shown in Fig. 12 and four corresponding cross sections of oceanographic surveyed profiles in Fig. 13. The gross features of the two figures bear general agreement, except that the isotherms in the model output are much smoother than the observed isotherms. The major discrepancy occurs in the high-latitude region above 45°N where the simulated temperature is warmer. The 4°C isotherm never reaches the surface in the model as it does in the observed data. This is primarily a result of the annual mean atmospheric forcing conditions which are biased by northern summer observations. Warm air temperatures in high latitudes used as constrained boundary conditions result in a correspondingly warm oceanic temperature distribution in the subarctic region. The overadjustment of the convective mechanism in the unstable water column also affects the mixed-layer depth which is rather deep in the model.

Simulated salinity distributions for three levels— surface, 350 m and near the bottom (3000 m)—are
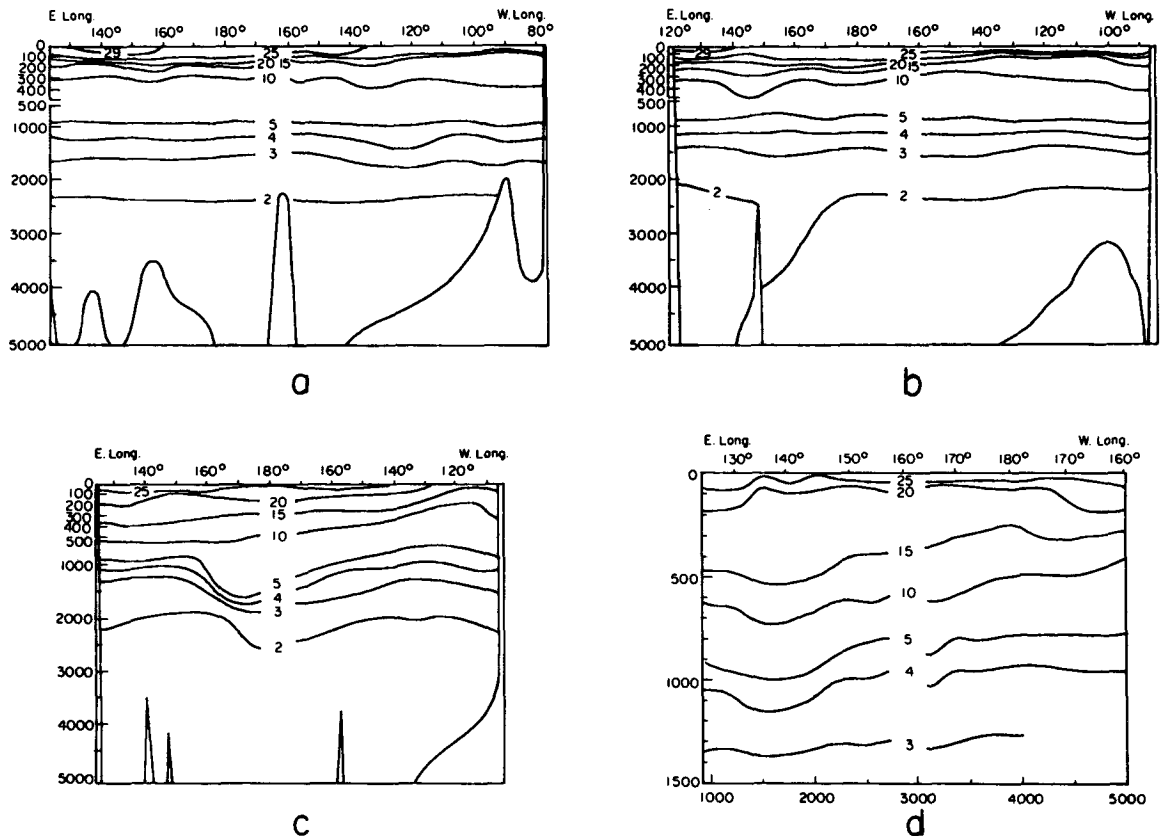

Fig. 11. Temperature (°C) profiles in east-west vertical cross-sections from observational data: (a) 0–10°N latitude; (b) 10–20°N latitude; (c) 20–30°N latitude (all from Muromtsev, 1963); (d) 35°N latitude (from Masuzawa, 1972).
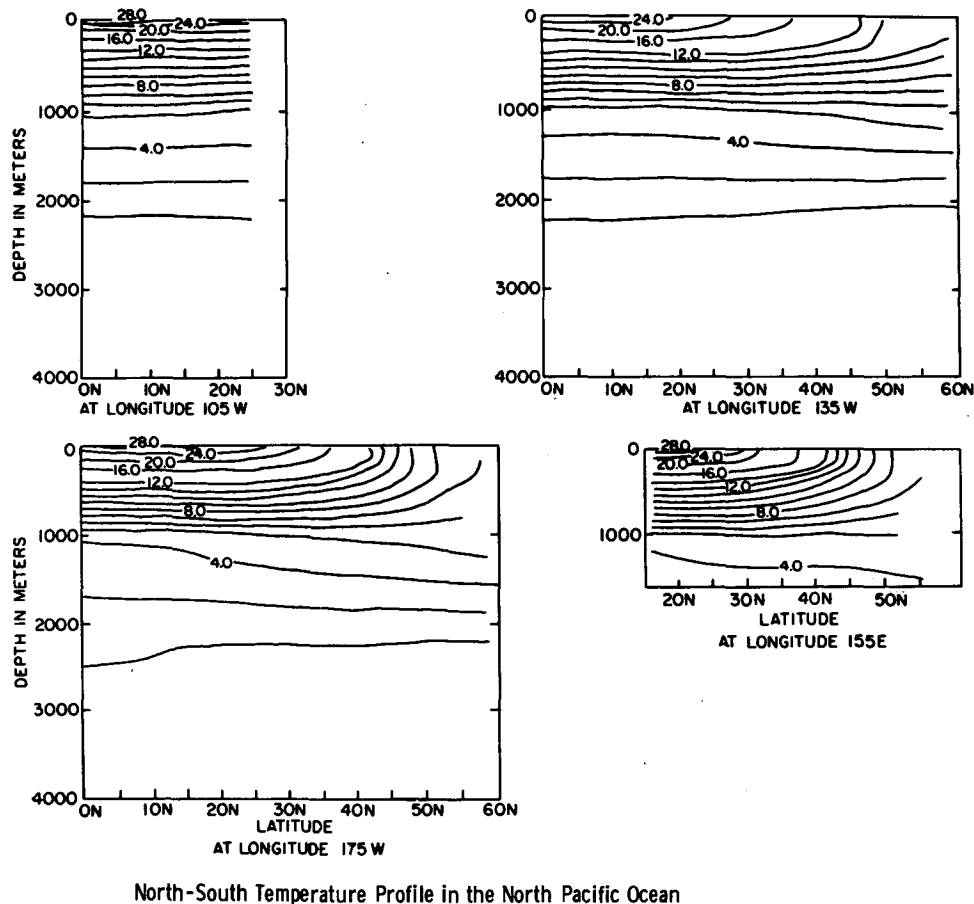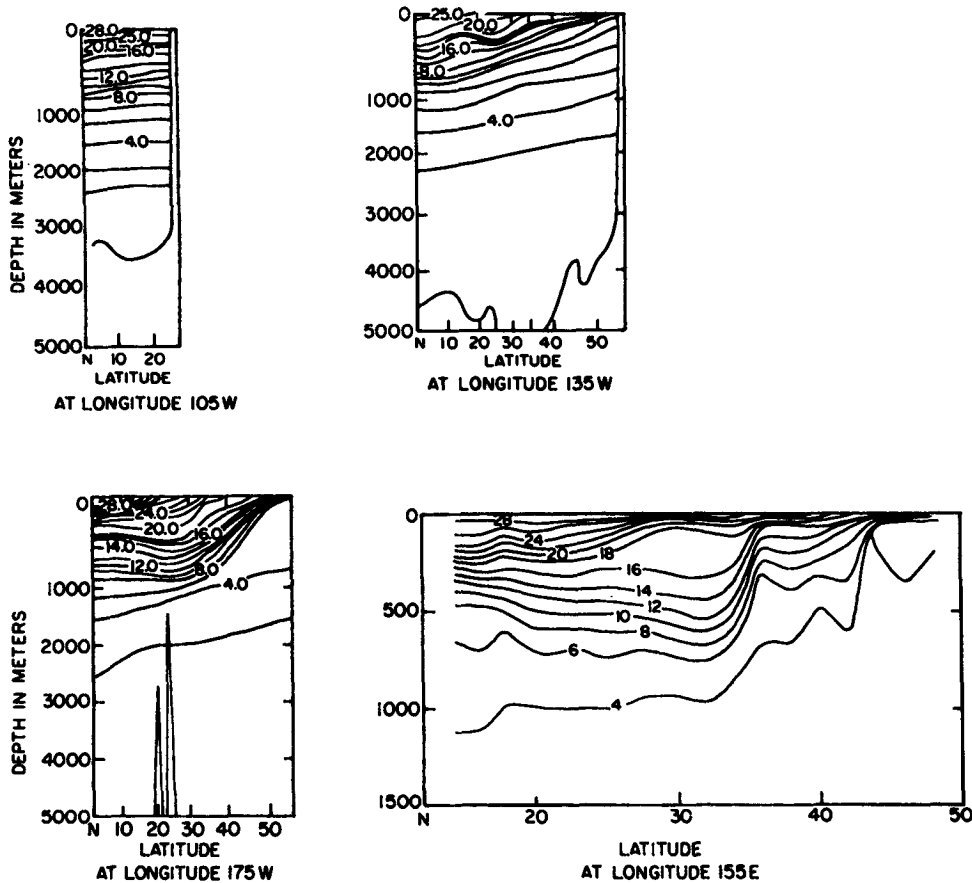
North-South Temperature Profile in the North Pacific Ocean

FIG. 12. Simulated temperature (°C) profiles in north-south vertical cross sections: (a) 105°W longitude; (b) 135°W longitude; (c) 175°W longitude; (d) 155°E longitude.

shown in Figs. 14a–14c, respectively. The surface salinity shows an elongated maximum zone above 35‰ between 20 and 30°N which declines poleward and equatorward as indicated in Fig. 14a. In the eastern tropics, there is also a high-salinity tongue near the boundary and extending westward. The north-south homogeneity is indicated in the western boundary region. At the depth of intermediate water level, salinity values are slightly higher, around 34.4 to 35.2‰, than those of the surface layer but with similar patterns as shown in Fig. 14b. The salinity in the bottom water is rather homogeneous with a slight high in the northwest. Reid's (1969) surface salinity distributions are shown in Fig. 15. General agreement in large-scale features exists between Figs. 14a and 15. Three meridional vertical cross sections at 180°, 105°W and 165°E are shown in Figs. 16a–16c, respectively, for the simulation, and in Figs. 17a–17c, for the observed atlas data (Muromtzev, 1963). There is qualitative agreement of the gross features for corresponding cross sections in Figs. 16 and 17. In the western North Pacific along 105°W, a maximum near 20°N and a

minimum near 5°N are shown in Figs. 16a and 17a. Along the 180° cross section, a large amount of low-salinity but high-density water sinking near 40°N to an intermediate water depth around 500 to 1000 m is clearly indicated in both Figs. 16b and 17b. There is a shallow salinity minimum in the vertical at a depth of around 100 m, a maximum at a depth of around 300 m, and a prominent minimum at the intermediate water depth. These features are also clearly shown in the eastern central North Pacific in both Figs. 16c and 17c. Certain discrepancies do exist between the simulated and the observed salinity distributions. The simulated salinity in the high-latitude region north of 40°N is about 1‰ higher than atlas data and the maximum salinity zone is closer to the eastern boundary than is the observed one. This is mostly caused by the inaccuracy of the evaporation and precipitation data imposed as the upper boundary condition. Recent studies (e.g., Reed and Elliot, 1973) have indicated that much higher precipitation occurs in the subarctic region than that given by Jacob (1951).

Observed North-South Cross-Section of Temperature Profile in the North Pacific Ocean

FIG. 13. Temperature (°C) profiles in the north-south cross sections from observational data: (a) 100–110°W longitude; (b) 130–140°W longitude; (c) 170–180°W longitude (all from Moromtsev, 1963); (d) 155°E longitude (from Masuzawa, 1972).

g. Pressure field and dynamic topography

The surface pressure can be calculated explicitly from the vertically integrated momentum equations

$$\left(\frac{p_0}{\rho_0}\right)_\lambda = \psi_{\phi t}\cos\phi + f\psi_\lambda - a\hat{G}\cos\phi - \frac{g}{\rho_0 D}$$

$$\times \int_{-D}^{0}\int_{z}^{0}\rho_\lambda\, dz'dz + a\hat{F}^\lambda\cos\phi, \quad (37)$$

$$\left(\frac{p_0}{\rho_0}\right)_\phi = \psi_{\lambda t}\sec\phi - f\psi_\phi - a\hat{G}^\phi - \frac{g}{\rho_0 D}$$

$$\times \int_{-D}^{0}\int_{z}^{0}\rho_\phi\, dz'dz + a\hat{F}^\phi, \quad (38)$$

where p_0 is the surface pressure and ψ the stream-function defined in (31) and (32). F and G are defined in (9), (10), (35) and (36). The p_0 can be obtained by integrations with an arbitrary constant appropriately adjusted with a known pressure point. Then

the pressure at all depths can be found by integrating the hydrostatic relation (29). An equivalent surface elevation η can be defined in terms of the surface pressure as

$$p_0 = p_a + \rho_0 g\eta, \quad (39)$$

where p_a is the atmospheric surface pressure.

The pressure field (divided by ρ_0) at the surface (10 m) and at the depths of 225 and 3000 m are shown in Fig. 18 in units of 0.1 m^2 s^{-2}. The pressure field (Fig. 18a) shows sharp horizontal gradients in the Kuroshio region, indicating a strong northward current. The pressure gradients outside of the boundary indicate a broad eastward flow in the midlatitudes and a weak southwestward flow in the tropics. At the depth of 225 m, the basic pattern of surface flow still exists at this depth but with more northward flow in the subarctic and more westward flow in the tropics. Near the bottom layer at a depth of 3000 m, the geostrophic circulation is opposite to that in the upper layers. There is south-
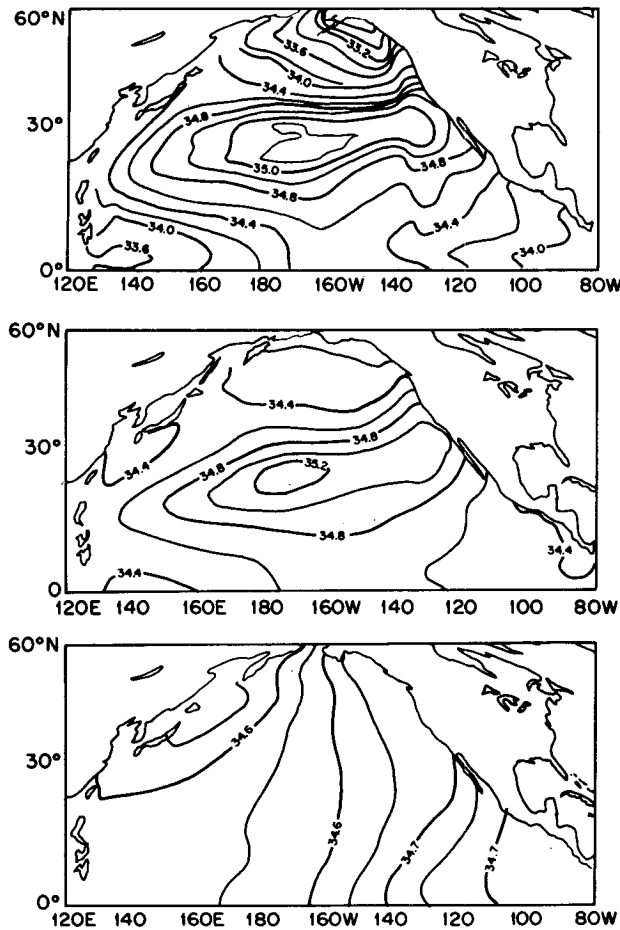
FIG. 14. Simulated salinity (‰) distributions of layers at depths of (a) 10 m; (b) 225 m; (c) 3000 m.

ward flow beneath the Kuroshio Current and a broad westward flow under the North Equatorial Current.

The annual mean dynamic topography of the sea surface with respect to 1000 db, as deduced by Wyrtki (1974) from observed density fields, is shown in Fig. 19. Although detailed information is not portrayed in the computed pressure field, especially near the equator, general features of the surface pressure (Fig. 18a), as interpreted in terms of the surface elevation, compare very favorably with annual mean dynamic topography in the North Pacific as shown in Fig. 19. Note that changes in the dynamic height in Fig. 19 correspond to changes in the surface pressure values in Fig. 18a divided by the gravitational acceleration, and the difference is just an arbitrary integration constant.

h. Energetics

The energy conservation for the model has been discussed briefly in the last paragraph of the formulation. The rate of change of kinetic energy per unit volume can be expressed symbolically as

$$K_t = \hat{K}_t + K_t' = \langle P \sim K \rangle + \langle \tau \rangle$$
$$+ \langle DV \rangle + \langle DW \rangle, \quad (40)$$

where $\hat{K}$ and K' are the rate of change of vertical mean and deviation from the mean kinetic energy per unit volume; $P \sim K$, the transformation between potential energy and kinetic energy due to the buoyancy effect; τ, the work done on the surface of the ocean by wind stress; DV, the dissipation of kinetic energy due to horizontal eddy viscosity; and DW, the dissipation of kinetic energy due to vertical eddy viscosity. The rate of change of potential energy per unit volume can be expressed as

$$P_t = \langle GP \rangle - \langle P \sim K \rangle + \langle DP \rangle, \quad (41)$$

where $P = \rho g(z + D)$ is the potential energy defined as before; GP denotes the advection of potential energy; $P \sim K$, the conversion of potential energy to kinetic energy; and DP, the diffusion of potential energy including all thermocline sources and sinks. Note that if integration is carried out for the whole mechanically closed domain, the advection effects such as GP contribute no work. However, redistribution of kinetic energy between the baroclinic mode K' and the barotropic mode $\hat{K}$ does occur because of the nonlinearity. Also conversion of potential to kinetic energy occurs only in the baroclinic mode because the ocean bottom is flat in the present study (Wiin-Nielsen, 1962; Holland, 1972).

The energetic diagram showing the magnitude and direction of work done per unit volume (ergs cm^{-1} day^{-1}), together with the total potential and the total barotropic and baroclinic energy (ergs cm^{-3}) are shown in Fig. 20. Potential energy is computed with reference to the ocean bottom. It is clear from Fig. 20 that the kinetic energy, from both the barotropic and the baroclinic modes, has reached a steady state but the potential energy is still losing energy at a rate of 2.5 ergs cm^{-3} day^{-1}. In the North Pacific, a major portion of the surface area is in the tropics and subtropics. This leads to a relatively large amount of input heat and output evaporation across the ocean surface as a whole. These net thermal and haline effects dominate the equilibrium potential energy state, the former decreasing the potential energy and the latter increasing it. As shown in the energy diagram, the thermal effect is very influential. A small contribution to the potential energy change is due to the net upwelling induced by the mechanical input of wind stresses. As pointed out by Haney (1974), consistent with Holland's (1972) result, the energy transformation is from potential to kinetic energy when the thermal boundary layer is greater than the viscous boundary layer as it is in the case of the present model, based on scale considerations. The vertical
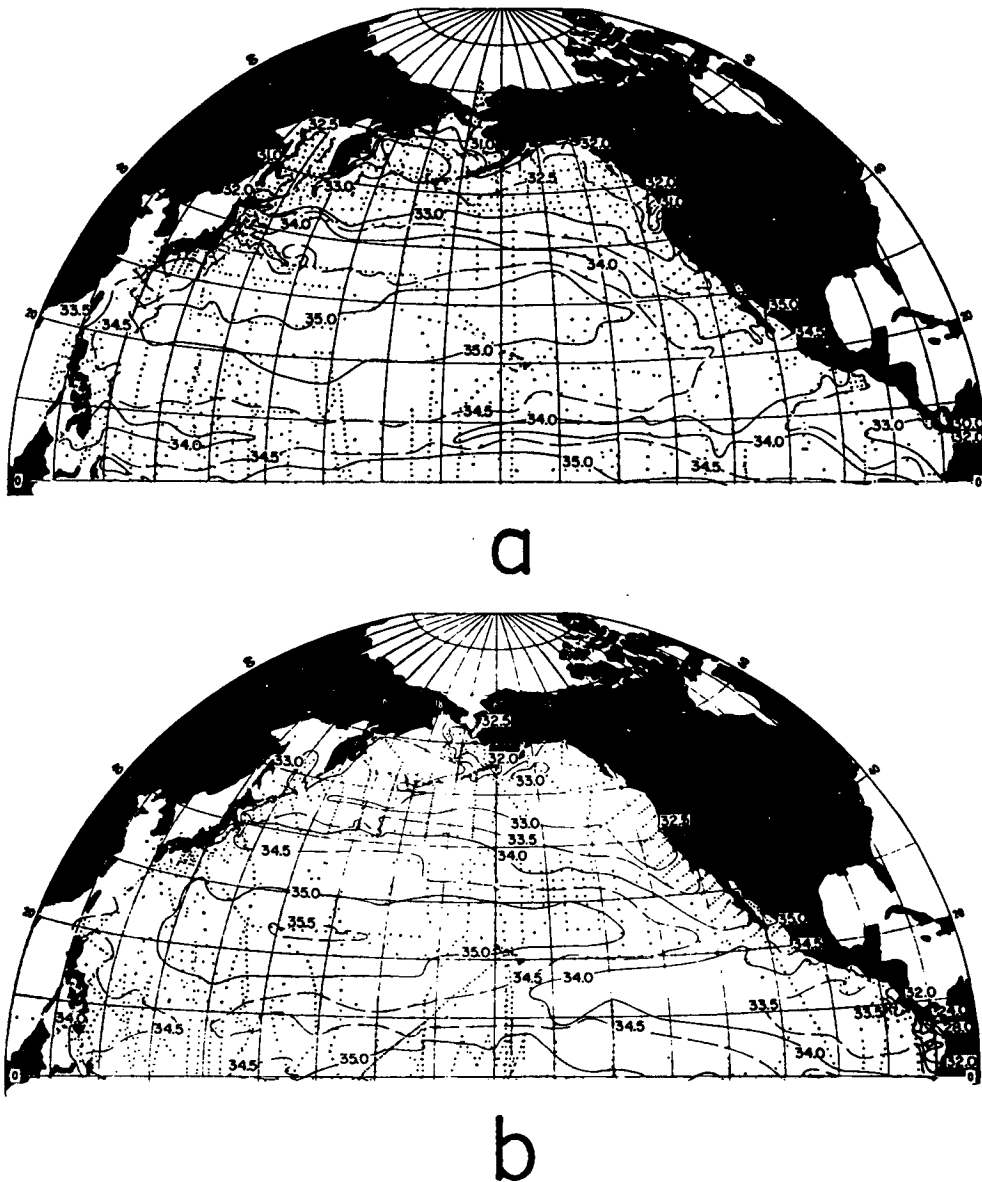
Fig. 15. Observed sea surface salinity (‰) in North Pacific Ocean (from Reid, 1969): (a) average summer; (b) average winter.

diffusive effects also result in an increase of the potential energy. Since the model has reached a quasi-equilibrium state, the energy loss due to the convective adjustments under unstable conditions is small. The kinetic energy is derived from the surface wind. Most of the mechanical energy input goes to the baroclinic mode. There is a small amount of energy conversion between the baroclinic mode and the barotropic mode due to the nonlinear effect.

i. Energy transport

One interesting and important problem in the numerical ocean simulation is that of finding out how much energy is transported by the ocean in the atmosphere/ocean system. In general, thermal energy must be transported poleward from low latitudes to high latitudes. The total northward transport of heat across a latitudinal circle in the ocean domain can be expressed as

$$H_T = \rho_0 C_p \int_{-D}^{0} \int_{\lambda_0}^{\lambda_I} \left[(\hat{v} + v')T \right.$$

$$\left. - \kappa_1 \frac{\partial T}{a \partial \phi} \right] a \cos\phi \, d\lambda dz, \quad (42)$$

where terms in the square brackets are the baro-
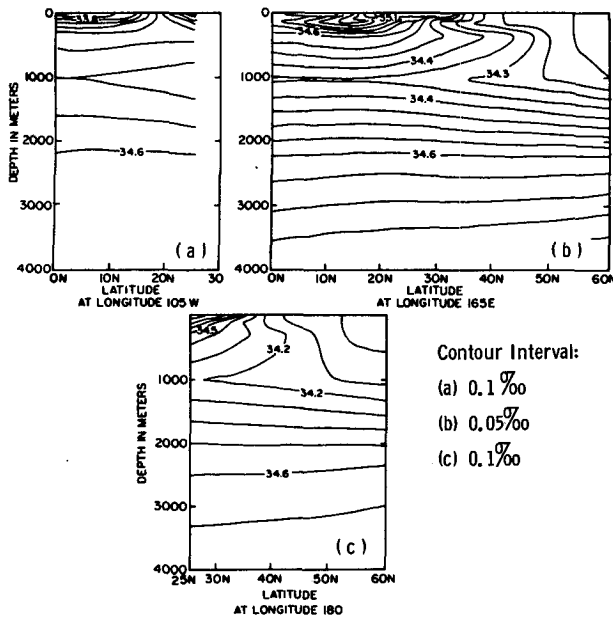
North-South Salinity Profile in the North Pacific Ocean

FIG. 16. Simulated salinity (‰) profiles in north-south vertical cross sections at (a) 105°W longitude; (b) 165°E longitude; (c) 180°W longitude.
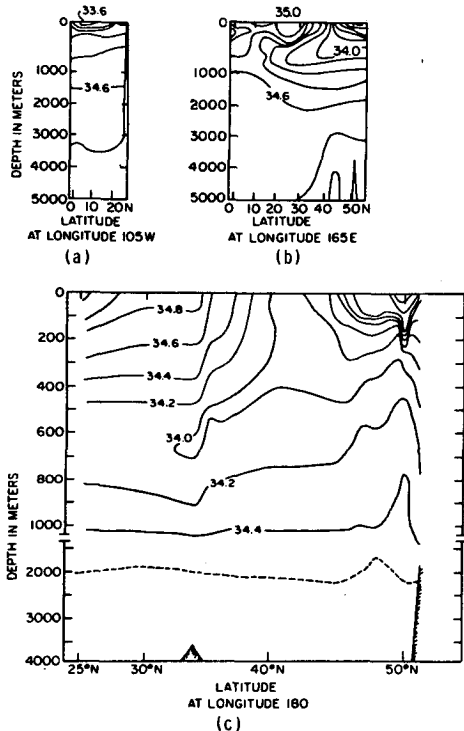
Observed North-South Salinity Profile in the North Pacific Ocean

FIG. 17. Observed salinity (‰) profiles in the north-south vertical cross sections: (a) 100°–110°W longitude; (b) 160°–170°W longitude (all from Muromtsev, 1963); (c) 180°W longitude (from Muromtsev, 1963).
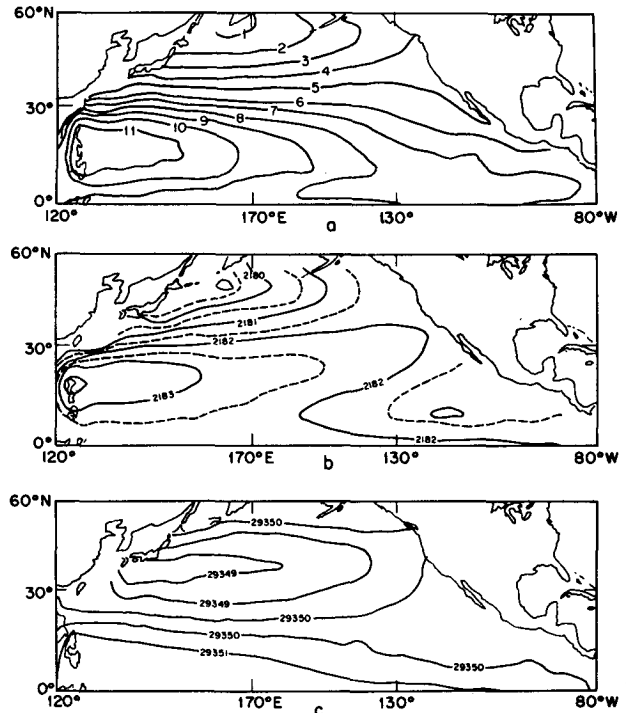

FIG. 18. Simulated pressure distributions: (a) at surface; (b) at 225 m/depth; (c) at 3000 m/depth. Contour interval is 0.1 m^2 s^{-2}.

tropic and baroclinic parts of the meridional velocity and the north-south diffusion due to the temperature gradient, and λ_0 and λ_1 are the longitudes of the western and the eastern boundaries, respectively. The results are shown in Fig. 21. Most of the poleward thermal energy in the tropics and subtropics is transported by the baroclinic advection which has approximately the same magnitude as the energy transported by the total current. The diffusion of heat contributes relatively little in low and high latitudes and is mostly equatorward in the tropics. However, in the midlatitude region where the meridional temperature gradient is large and the current is mostly zonal, the transport of heat energy by diffusive processes is important. The total rate of the northward thermal energy transport is about 2 × 10^{14} cal s^{-1} (8.37 × 10^{14} W). Maximum transports occur at latitudes between 10 and 25°N.

There are numerous previous studies of the poleward energy transport by ocean currents (e.g., Sverdrup, 1957; Budyko, 1958; Bryan, 1962). One of the most recent is that of Vonder Haar and Oort (1973) who estimated the annual poleward energy transport based on recent measurements of the earth's radiation budget from satellites, together with atmospheric energy transport summaries based on rawinsonde data. Their results for the oceanic poleward transport of heat in the Northern Hemisphere are shown in Fig. 22. The mean peak oceanic heat
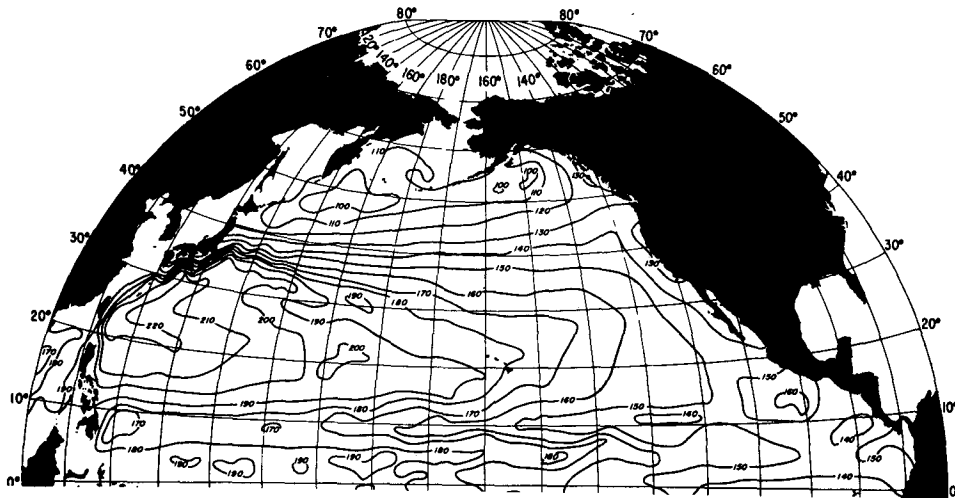
FIG. 19. Annual mean dynamic height of sea surface in dynamic cm with respect to 1000 m reference level (from Wyrtki, 1974).

transport (2.5 × 10²² cal year⁻¹ or 3.32 × 10¹⁵ W) for the North Pacific, the North Atlantic and the North Indian Oceans together occurs near 20°N and accounts for 74% of the energy transport at that latitude. On the average, the oceans contribute about 40% in the Northern Hemisphere of the required energy transport in the atmosphere/ocean/earth system. Sellers' (1965) similar estimation based on the surface energy budget of Budyko (1963) is also shown in Fig. 22 as BS. As pointed out by Vonder Haar and Oort, Sellers' estimate is relatively lower. The computed energy transport in the North Pacific Ocean model, indicated as NPO, is also shown in Fig. 22. Although quantitative comparison between the observational estimates and the model output excluding the energy transport from the Atlantic and Indian Oceans is not meaning-

ful, it is certain that the total simulated oceanic energy transport including the above-mentioned transports would be closer to the recent estimate by Vonder Haar and Oort (1973).

5. Summary and conclusions

Based on Haney's (1974) idealized basin model, a North Pacific Ocean model has been developed for the study of the physical nature and dynamic response of large-scale, long-term fluctuations in
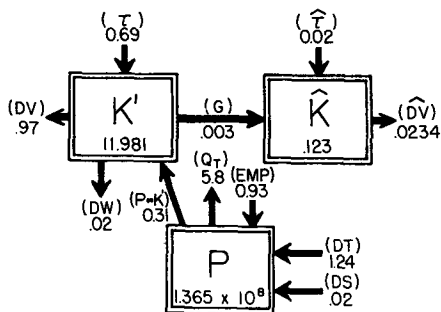

FIG. 20. Energetic diagrams in the NORPAX model. Units for energy are ergs cm⁻³, and for rates of energy transformation, ergs cm⁻³ day⁻¹. P denotes potential energy; $\hat{K}$, barotropic energy; K', baroclinic energy; τ, wind stresses; G, nonlinear energy transformation; DV, horizontal diffusion of energy; DW, vertical diffusion of energy; (p ~ k), energy transformation between P and K; Q_T, heat energy input; (EMP), energy input due to evaporation and precipitation differences; DT and DS, potential energy diffusion.

□—□ Total northward heat transport
△—△ Heat transport by total current
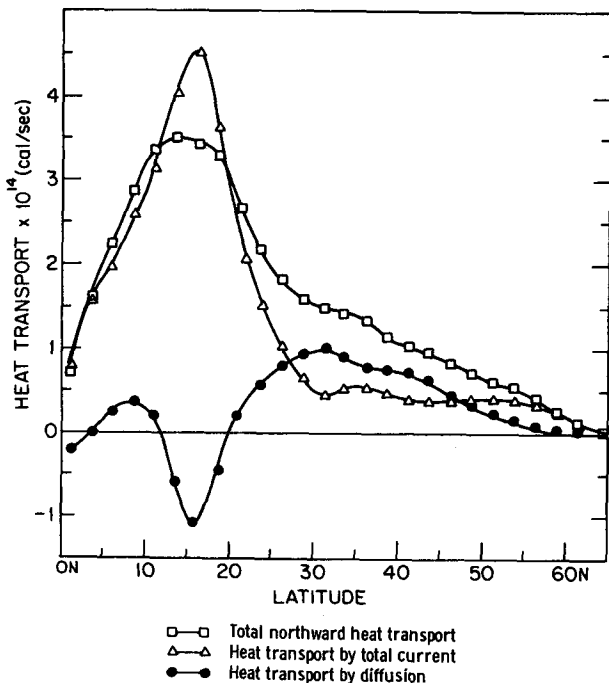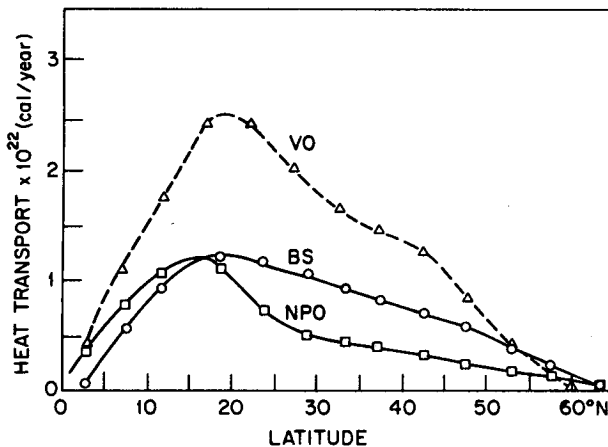●—● Heat transport by diffusion

FIG. 21. Zonally averaged meridional heat transport in the model.

Variation of Northward thermal energy transport in the North Pacific Ocean
NPO computed from the NORPAX Ocean Model
BS   Ocean energy transport according to Budyko (1963) and Sellers (1965)
VO   Ocean energy transport estimated by Vonder Haar and Oort (1973)

FIG. 22. Total meridional heat transport in the north hemisphere. Curve VO is the total heat transport from Vonder Haar and Oort (1973); curve BS, from Budyko (1963) and Sellers (1965), and curve NPO is the heat transport computed from the NORPAX model for the North Pacific Ocean alone. (Note: 1 cal s^{-1} = 4.1855 W; 1 cal year^{-1} = 1.33 × 10^{-7} W).

cyclonic gyres in the tropic and subarctic regions, respectively, similar to the solutions of a diffusive ocean (Munk, 1950). Layer-by-layer velocity patterns show surface flow toward the west and deep flow toward the east near the equator, indicating the simulation of the South Equatorial Current and the Equatorial Undercurrent. There is a northward Kuroshio Current above 700 m and a returning southward flow underneath it. The layer-by-layer streamline patterns show large-scale anticyclonic circulations above 1000 m and opposite patterns below. There is strong upwelling near the equator and at the western boundary in the upper two layers and downwelling in the lower layers in the equatorial region. The simulated gross nature of the temperature and salinity distributions compare well with observed field atlas data. The surface pressure field also compares satisfactorily with dynamic height distribution based on density observations. The northward transport of thermal energy is accomplished primarily by the baroclinic current, and the total thermal energy transport is rather large (1·1 × 10^{22} cal year^{-1} or 1.46 × 10^{15} W). However, both temperature and salinity values from the model are higher than observed mean data in high latitudes. This is mostly due to the higher annual mean air temperature and lower evaporation and precipitation values imposed upon the model than those in the real atmospheric field.

In spite of obvious shortcomings, such as no bottom topography and a rather coarse grid, the present regional North Pacific model has demonstrated its ability to portray the large-scale mean circulation patterns and mean density fields in the North Pacific. Later papers will deal with the response to time-dependent forcing.

the North Pacific Ocean. During the first stage of time integration, a coarse grid mesh with horizontal separation of 5° and seven layers was used to obtain the long-term mean state of the circulation. In the second stage, the model was refined to 2.5° in horizontal separations with 10 layers in the vertical. Annual mean observed atmospheric data were imposed as the upper boundary conditions. After about 60 years of integration in the second phase, a quasi-equilibrium state in the ocean was reached. The present paper deals with the long-term mean state after the completion of the second phase.

Dynamic analyses show that geostrophic balance is approximately maintained in the interior ocean as expected. In the surface layer, the momentum balances are controlled by Ekman dynamics. The nonlinear terms are generally small but not negligible. In the heat and salinity equations, the convergence of the advective fluxes of heat and salinity are the dominating terms. This leads to the question as to how accurately the energy budget in a measurable volume of water in the real ocean can be calculated. Since the horizontal and vertical fluxes tend to balance, small errors involved in the measurement of the transports, especially the vertical one, may result in large residual errors in the heat budget.

The vertically integrated streamfunction shows three gyre circulators in the North Pacific Ocean, one anticyclonic gyre in the subtropics, and two

REFERENCES

Allen, J., 1964: A description report on the physical and chemical properties of the north-western Pacific Ocean during summer 1963. U. S. Naval Oceanographic Office, No. 0-17-64.

Arakawa, A., 1966: Computational design for long-term numerical integration of the equations of fluid motion: two-dimensional incompressible flow, Part I. *J. Comput. Phys.*, **1**, 119–143.

Arthur, R. S., 1966: Estimation of mean monthly anomalies of sea-surface temperature. *J. Geophys. Res.*, **71**, 2689–2690.

Bjerknes, J., 1962: Synoptic survey of the interaction of sea and atmosphere in the North Atlantic. *Geofys. Publik.*, **24**, 11–145.

——, 1966: A possible response of the atmospheric Hadley circulation to equatorial anomalies of ocean temperature. *Tellus*, **19**, 830–829.

——, 1969: Atmosphere teleconnections from the equatorial Pacific. *Mon. Wea. Rev.*, **47**, 162–172.

Bryan, K., 1962: Measurements of meridional heat transport by ocean currents. *J. Geophys. Res.*, **67**, 3403–3414.

——, 1963: A numerical investigation of a nonlinear model of a wind-driven ocean. *J. Atmos. Sci.*, **20**, 594–606.

——, 1969: A numerical method for the study of the circulation of the world ocean. *J. Comput. Phys.*, **4**, 347–376.

——, and M. D. Cox, 1968: A nonlinear model of an ocean driven by wind and differential heating: Part I and part II. *J. Atmos. Sci.*, **25**, 945–978.

——, and ——, 1972: The circulation of the world ocean: a numerical study. Part I, a homogeneous model. *J. Phys. Oceanogr.*, **2**, 319–335.

——, S. Manabe, and R. C. Pacanowski, 1975: A global ocean-atmosphere climate model. Part II. The ocean circulation. *J. Phys. Oceanogr.*, **5**, 30–46.

Budyko, M. I., 1958: *The Heat Balance of the Earth's Surface*. U. S. Weather Bureau, Washington, DC, 259 pp. [English Translation].

——, 1963: *Atlas of the Heat Balance of the Globe* (in Russian). Moscow, Hydrometeorological Service, 69 pp.

Businger, J. A., J. C. Wyngaard, Y. Izumi and E. F. Bradley, 1971: Flux-profile relationships in the atmospheric surface layer. *J. Atmos. Sci.*, **28**, 181–189.

Bye, J. A. T., and T. W. Sag, 1972. A numerical model for circulation in a homogeneous world ocean. *J. Phys. Oceanogr.*, **2**, 305–318.

Cox, M. E., 1970: A mathematical model of the Indian Ocean. *Deep-Sea Res.*, **17**, 47–75.

Crowley, W. P., 1970: A numerical model for viscous, free-surface barotropic wind driven ocean circulation. *J. Comput. Phys.*, **5**, 139–168.

Deardorff, J. W., 1968: Dependence of air-sea transfer coefficients on bulk stability. *J. Geophys. Res.*, **73**, 2549–2557.

Gates, W. W., E. S. Batten, A. B. Kahle and A. B. Nelson, 1971: A documentation of the Mintz-Arakawa two-level atmospheric general circulation model. Advance Research Project Agency Report R-877-ARPA, Rand Corporation, 408 pp.

Gill, A. E., and P. P. Niiler, 1973: The theory of the seasonal variability in the ocean. *Deep-Sea Res.*, **20**, 141–177.

Gormatyuk, Yu.K., and A. W. Sarkisyan, 1965: Results of four-level model calculations of North Atlantic currents. *Izv. Atmos. Oceanic Phys. Ser.* 1, **3**, 313–326.

Haney, R. L., 1974: A numerical study of the response of an idealized ocean to large-scale surface heat and momentum flux. *J. Phys.Oceanogr.*, **4**, 145–167.

——, and R. W. Davies, 1976: The role of surface mixing in the seasonal variation of the ocean thermal structure. *J. Phys. Oceanogr.*, **6**, 504–510.

Hata, K., 1965: Seasonal variation of the volume transport in the Oyashio area. *J. Oceanogr. Soc. Japan*, **21**, 193–201.

Hellerman, S., 1967: An updated estimate of the wind stress on the world ocean. *Mon. Wea. Rev.*, **95**, 607–626. (see Corrigendum, *Mon. Wea. Rev.*, **96**, 63–74).

Hess, S. L., 1959: *Introduction to Theoretical Meteorology.* Holt, Rinehart and Winston, 355 pp.

Holland, W. R., 1967: On the wind driven circulation in an ocean with bottom topography. *Tellus*, **19**, 582–599.

——, 1972: Energetics of baroclinic oceans. Paper presented at the Symposium on Numerical Models of the Ocean Circulation, Durham, NH, 17–20 October.

——, and A. L. Hirschman, 1973: A vertical calculation of the circulation in the North Atlantic Ocean. *J. Phys. Oceanogr.*, **2**, 336–354.

——, and L. B. Lin, 1975: On the generation of mesoscale eddies and their contribution to the oceanic general circulation. Part I and II. *J. Phys. Oceanogr.*, **2**, 336–354.

Huang, J. C. K., 1973. A multi-layer, nonlinear regional dynamic model of the North Pacific Ocean. S10 Ref. 73-23, Scripps Institution of Oceanography, 45 pp.

——, W. Shaw and C. J. Shieh, 1977: A brief documentation of the NORPAX ocean model. ONR Report, Dept. Atmos. and Ocean. Science, The University of Michigan, 245 pp.

Il'in, A. M., V. M. Kamenkovich, R. G. Zhugvina and M. M. Silkina, 1969: On the calculation of complete circulation in the world ocean. *Izv Atmos. Oceanic Phys.*, **5**, 1160–1171.

Isaacs, J. D., 1968: Probing the birthplace of American weather. *Naval Research Reviews*, ONR, Washington, DC, 13 pp.

Jacob, W. C., 1951: The energy exchange between sea and atmosphere and some of its consequences. *Bull. Scripps Inst. Oceanogr.*, **7**, 27–122.

——, 1967: Numerical semiprediction of monthly mean sea-surface temperature. *J. Geophys. Res.*, **72**, 1681–1689.

Johnson, T. H., G. A. Flittner and M. W. Cline, 1958: Automatic data processing program for marine synoptic radio weather reports. Spec. Sci. Rep. 503, Bureau of Commercial Fisheries, 74 pp.

Lilly, D. K., 1965: On the computational stability of numerical solutions of time-dependent nonlinear geophysical fluid dynamics problems. *Mon. Wea. Rev.*, **93**, 11–26.

London, J., 1957: A study of the atmospheric heat balance. Final report, AF19(122)-165, Dept. Meteor. Oceanogr., New York University, 99 pp.

Manabe, S., and K. Bryan, 1969: Climate calculations with a combined ocean-atmosphere model. *J. Atmos. Sci.*, **24**, 241–259.

——, K. Bryan and M. Spelman, 1975: A global ocean-atmosphere climate model. Part I, The atmosphere circulation. *J. Phys. Oceanogr.*, **5**, 3–29.

Masuzawa, J., 1972: Water characteristics of the North Pacific central region. *Kuroshio*, H. Stommel and K. Yoshia, Eds., University of Washington Press (see pp. 95–116).

Matsuno, T., 1966: Numerical integrations of the primitive equations by a simulated backward difference method. *J. Meteor. Soc. Japan*, Ser. 2, **44**, 76–84.

Muromtsev, A., 1963: *The Principal Hydrological Features of the Pacific Ocean*. Gidrometeoizdat, 417 pp. [Translated by Israel Program for Scientific Translations, Jerusalem].

Munk, W. H., 1950: On the wind-driven ocean circulation. *J. Meteor.*, **7**, 79–93.

Namias, J., 1959: Recent seasonal interactions between North Pacific water and the overlying atmosphere condition. *J. Geophys. Res.*, **64**, 631–646.

——, 1965: Macroscopic association between mean monthly sea-surface temperature and the overlying winds. *J. Geophys. Res.*, **70**, 2307–2318.

——, 1970: Macroscale variations in sea-surface temperature in the North Pacific. *J. Geophys. Res.*, **75**, 565–582.

Nitani, H., 1972: Beginning of the Kuroshio. *Kuroshio*, H. Stommel and K. Yoshida, Eds., University of Washington Press (see pp. 129–163).

O'Brien, James J., 1971: A two-dimensional model of the wind-driven North Pacific. *Invest. Pesquera*, **35**, 331–349.

Petterssen, S., D. L. Bradbury and K. Pedersen, 1962: The Norwegian cyclone models in relation to heat and cold sources. *Geofys. Publik.*, **24**, 243–280.

Reed, R. K., and W. P. Elliot, 1973: Precipitation of ocean weather stations in the North Pacific. *J. Geophys. Res.*, **78**, 7087–7091.

Reid, J. L., 1969: Sea surface temperature salinity and density of the Pacific Ocean in summer and winter. *Deep-Sea Res.*, **16**, (Suppl.) 215–224.

——, 1973: *Northwest Pacific Ocean Water in Winter*. The Johns Hopkins University Press, 96 pp.

Robinson, A. R., D. E. Harrison, Y. Mintz and A. J. Semtner, 1977: Eddies and the general circulation of an idealized oceanic gyre: A wind and thermally driven primitive equation numerical experiment. *J. Phys. Oceanogr.*, **7**, 182–207.

Rodewald, M., 1963: Sea-surface temperature of the North Atlantic Ocean during the decade 1951–1960, their anomalies and development in relation to the atmosphere circulation. *Arid Zone Res.*, **20**, 97–107.

Sellers, W. D., 1965: *Physical Climatology*. University of Chicago Press, 272 pp.

——, 1957: *Oceanography. Handbuch der Physik*, Vol. 48. Akademe-Verlag, (see pp. 608–670).

——, M. W. Johnson and R. H. Fleming, 1942: *The Oceans, Their Physics, Chemistry and General Biology*. Prentice-Hall, Inc., 1087 pp. (see p. 723).

Takano, K., 1969: General circulation in the global ocean. *J. Oceanogr. Soc. Japan*, **25**, 48–50.

——, 1975: Eddy viscosity and grid size in ocean models. *J. Oceanogr. Soc. Japan*, **31**, 105–108.

Vonder Haar, T. H., and K. J. Hanson, 1969: Absorption of solar radiation in tropical regions. *J. Atmos. Sci.*, **26**, 652–655.

——, and A. H. Oort, 1973: New estimate of annual poleward energy transport by Northern Hemisphere oceans. *J. Phys. Oceanogr.*, **3**, 169–172.

Warren, B. A., 1963: Topographical influence in the path of the Gulf Stream. *Tellus*, **15**, 167–183.

Wiin-Nielson, A., 1962: On transformation of kinetic energy between the vertical shear flow and the vertical mean flow in the atmosphere. *Mon. Wea. Rev.*, **90**, 311–323.

White, W. B., 1975: Secular variability in the large-scale baroclinic transport of the North Pacific from 1950 to 1970. *J. Mar. Res.*, **33**, 141–145.

Wyrtki, K., 1974: The dynamic topography of the Pacific Ocean and its fluctuations. HIG-74-5, Hawaii Inst. Geophys., 26 pp.